iScience

CellPress
OPEN ACCESS

Article

Roquin-1 resolves sepsis-associated acute liver injury by regulating inflammatory profiles via miRNA cargo in extracellular vesicles

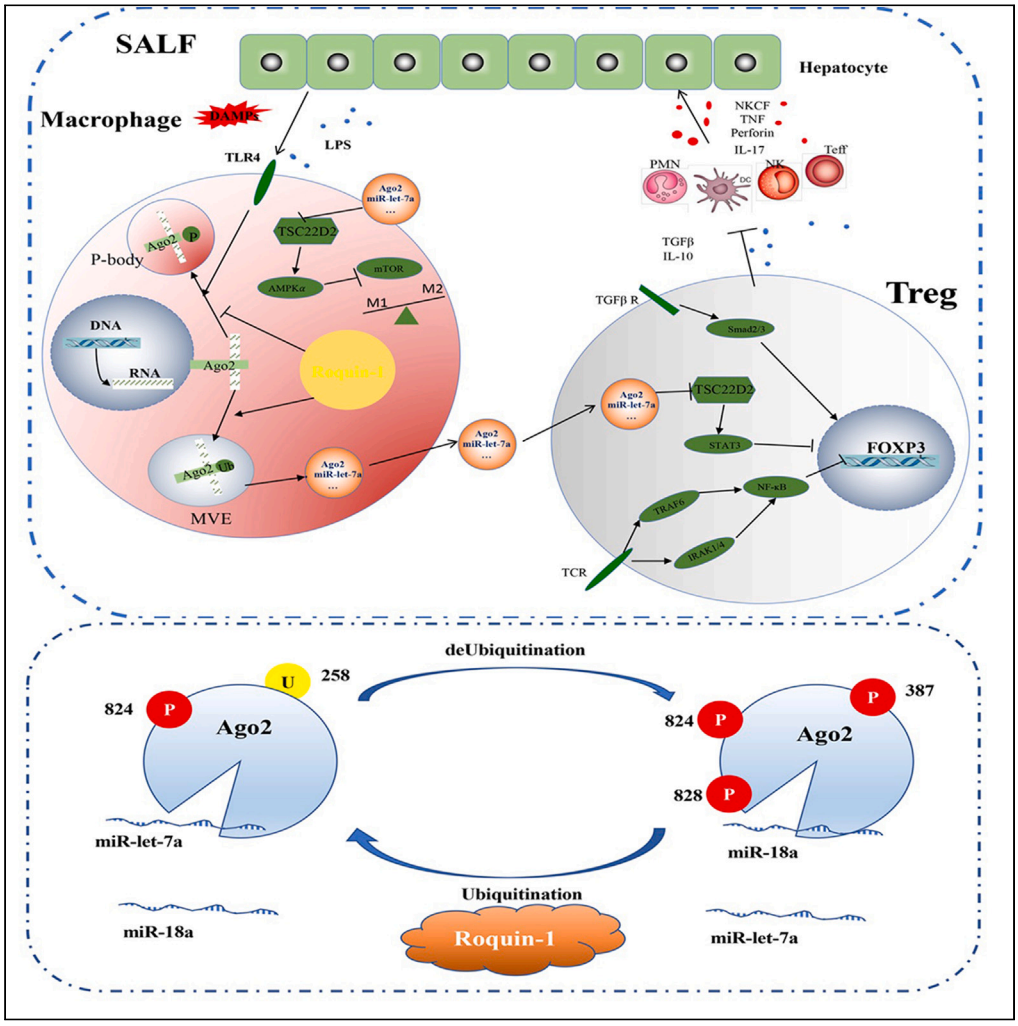

Lei Zheng, Wei Ling, Deming Zhu, Zhi Li, Yousheng Li, Haoming Zhou, Lianbao Kong

gisurgery@qq.com (Y.L.)
hmzhou@njmu.edu.cn (H.Z.)
lbkong@njmu.edu.cn (L.K.)

Highlights

The mechanism of ALF involves innate and adapted immunity

Roquin-1 modulates miRNA sorting in macrophages derived extracellular vesicles

The miRNA in macrophage derived extracellular vesicles regulates Tregs differentiation

Zheng et al., iScience 26, 107295
August 18, 2023 © 2023
https://doi.org/10.1016/j.isci.2023.107295

iScience

CellPress
OPEN ACCESS

Article

Roquin-1 resolves sepsis-associated acute liver injury by regulating inflammatory profiles via miRNA cargo in extracellular vesicles

Lei Zheng,[1,2] Wei Ling,[1] Deming Zhu,[1] Zhi Li,[1] Yousheng Li,[2,3,*] Haoming Zhou,[1,3,*] and Lianbao Kong[1,3,4,*]

SUMMARY

Sepsis-associated acute liver injury (SALI) is an independent risk for sepsis-induced death orchestrated by innate and adaptive immune responses. Here, we found that Roquin-1 was decreased during SALI and expressed mainly in monocyte-derived macrophages. Meanwhile, Roquin-1 was correlated with the inflammatory profiles in humans and mice. Mechanically, Roquin-1 in macrophages promoted Ago2-K258-ubiquitination and inhibited Ago2-S387/S828-phosphorylation. Ago2-S387-phosphorylation inhibited Ago2-miRNA's complex location in multivesicular bodies and sorting in macrophages-derived extracellular vesicles (MDEVs), while Ago2-S828-phosphorylation modulated the binding between Ago2 and miRNAs by special miRNAs-motifs. Then, the anti-inflammatory miRNAs in MDEVs decreased TSC22D2 expression directly, upregulated Tregs-differentiation via TSC22D2-STAT3 signaling, and inhibited M1-macrophage-polarization by TSC22D2-AMPKα-mTOR pathway. Furthermore, WT MD EVs in mice alleviated SALI by increasing Tregs ratio and decreasing M1-macrophage frequency synchronously. Our study showed that Roquin-1 in macrophages increased Tregs-differentiation and decreased M1-macrophage-polarization simultaneously via miRNA in MDEVs, suggesting Roquin-1 can be used as a potential tool for SALI treatment and MDEVs engineering.

INTRODUCTION

Sepsis, a life-threatening organ dysfunction due to the abnormal response to infection, is a significant cause of death in hospitalized patients and a direct result of improved healthcare for patients with various diseases.[1] Moreover, sepsis develops rapidly due to the multidirectional response to external/endogenous factors and concomitant conditions.[2] The sepsis-induced inflammatory response can lead to multiple organ dysfunction, including in the heart, lung, liver, kidney, and so on.[3] Dysfunction of one or two organs was diagnosed in 10% of patients at the time of admission, whereas most patients developed dysfunction of three or more organs during their ICU stay.[4] The liver can inhibit the elimination of bacteria-derived products and endotoxin, which are involved in the appropriate local cytokine response and promote direct translation of injurious consequences into the systemic circulation.[5] Therefore, sepsis-associated acute liver injury (SALI) may aggravate sepsis-related disease prognosis.[6] Liver dysfunction is an available therapeutic target to improve the prognosis of severe sepsis-related diseases. However, the particular therapeutic method to treat SALI is currently unavailable.

The balance of innate and adaptive immune resection plays an essential role in SALI.[7,8] Macrophages (møs), critical for preventing spreading infections, play a crucial role in keeping liver homeostasis in SALI.[9–12] Meanwhile, the absence of regulatory T cells (Tregs) inhibited the hepatoprotective effects of mesenchymal stem cells.[7] Furthermore, the inflammatory processes in the liver and distant organs are determined by the diverse interactions between møs and other immune cells, cytokines, and other humoral substances.[13] However, this intercellular network reaches a level of complexity that has not been fully comprehended until date.

Roquin-1, a ubiquitin regulator, was a point mutation causing systemic lupus erythematosus disease.[14] Roquin-1 contains a unique HEPN domain and identifies the structural basis of the 'san' mutation and Roquin's ability to bind multiple RNAs. Roquin-1 emerges as a protein that can bind Ago2, miRNAs, and

[1]Hepatobiliary Center/Liver Transplantation Center, The First Affiliated Hospital of Nanjing Medical University, 300 Guangzhou Road, Nanjing 210029, P.R. China

[2]Department of General Surgery, Shanghai Ninth People's Hospital, Shanghai Jiao-tong University School of Medicine, 639 Zhizaoju Road, Shanghai 200011, P.R. China

[3]These authors contributed equally

[4]Lead contact

*Correspondence: gisurgery@qq.com (Y.L.), hmzhou@njmu.edu.cn (H.Z.), lbkong@njmu.edu.cn (L.K.)

https://doi.org/10.1016/j.isci.2023.107295

target mRNAs, to control homeostasis of both RNA species.[15] In antitumor response and immune-related conditions, Roquin-1 regulated the function of T helper cells, B cells, and autoantibody production.[16–18] Our previous study determined that Roquin-1 upregulated the ubiquitination of AMPKα and inhibited its phosphorylation.[19] However, the role of Roquin-1 in møs during SALI is still unexplored.

The discovery of the intercellular signaling capabilities of extracellular vesicles (EVs) has opened up new avenues for modulating møs and T cell phenotypes, which we investigated in our work. EVs are categorized according to size, subcellular origin, shape, and collecting techniques. EVs play a critical role in intercellular communication and serve as a biomarker and tools for diagnosing and treating diseases.[20] Multiple organs can release EVs during sepsis, including the heart, lungs, liver, and nervous system.[16] EVs contain several intercellular signaling cargo molecules, including mRNAs, miRNAs, lncRNAs, proteins, and lipids. The hepatocytes took LPS- treated møs derived EVs and increased AST and ALT in serum.[21] Therefore, EVs have the potential to operate as indicators and therapeutic agents, notably in immune-related diseases, and are thus the subject of significant attention. However, the impact of macrophage-derived extracellular vesicles (MDEVs) has been controversial, with either proinflammatory or anti-inflammatory functions. According to numerous studies, endothelial cells and activated monocytes or møs released EVs that spread pro-inflammatory signals using a variety of different ways.[22] Meanwhile, anti-inflammatory microRNA-99a/146b/378a was present in MDEVs and promoted M2 polarization in recipient møs and inhibit inflammation by targeting NF-B and TNF-signaling.[23] But once released out of the source cells, the specific role of these immune cell derived EVs and the effects of their microRNA are still poorly understood. Further studies are awaited to confirm the role of MDEVs in SALI.

In the present study, we identified a protein, Roquin-1, significantly downregulated in monocyte-derived møs in SALI patients and the experimental mouse models. We found that Roquin-1$^{san/san}$ (san roque mutation, a kind of point mutation) in monocyte-derived møs modulated selected miRNA sorting in MDEVs, promoted M1 polarization and inhibited Tregs differentiation synchronously *in vitro* and vivo. The favorable qualities imparted by wildtype (WT) and Roquin-1$^{san/san}$ MDEVs, as well as their ease of generation and modification of miRNA cargo, provide a novel therapeutic route for the treatment of immune-related diseases, including SALI.

RESULTS

Roquin-1 is expressed by monocyte-derived macrophage in WT mice with SALI

Little is known about the effect of Roquin-1 on liver function during SALI, so we used D-GALN and LPS to establish the SALI model and assessed markers of liver injury (alanine transaminase (ALT)/aspartate aminotransferase (AST) in serum, hematoxylin-eosin stains (HE stains) and Suzuki's scores) in WT mice. The results showed a significant elevation of these markers (ALT/AST/HE stains/Suzuki's scores) after D-GALN/LPS stimulation, peaking 7 h after SALI. At the same time, we found a significant difference in serum ALT/AST (Figure S1A) between the D-GALN+LPS group and the other three control groups (saline control, D-GALN, LPS). By comparing HE stains and Suzuki's scores (Figure S1B) at different times, we found that the liver injury in the D-GALN+LPS group at 7 h after SALI was the most serious. Therefore, we used GALN+LPS to build SALI model in mice for further research.

Then, according to RT-qPCR (Figure 1A), WB (Figure 1B) and immunohistochemistry (IHC) (Figure 1C) in the liver, we found that the expression of Roquin-1 increased at 5 h and reduced at 7 h significantly after SALI in mice. Meanwhile, the double-labeled immunofluorescence showed that F4/80+ møs were the primary source of Roquin-1 (Figure 1D). Furthermore, to determine the location of Roquin-1, we separated F4/80+ møs and hepatocytes and detected Roquin-1 in F4/80+ møs and hepatocytes. Roquin-1 in F4/80+ møs was increased at 5 h and reduced at 7 h after SALI (Figures 1E and S1C), while it did not express in hepatocytes (Figures S1D and S1E). Additionally, CX3CR1 (monocyte-derived møs marker) and Clec4F (tissue-resident møs marker) were used to investigate the primary source of Roquin-1. According to double immunofluorescence labeling (Figure 1F), Roquin-1 at 5 h after SALI was mainly expressed in CX3CR1+Clec4F- cells. Meanwhile, we separated the monocyte-derived møs (F4/80+CX3CR1+) and tissue-resident møs (F4/80+Clec4F+) and detected Roquin-1 expression. According to WB and RT-qPCR, Roquin-1 was mainly expressed in the CX3CR1+Clec4F- møs instead of CX3CR1-Clec4F+ møs (Figures 1G and S1F–S1H). Then, FACS analysis revealed CX3CR1+Clec4F- møs was the principal Roquin-1-expressing cells and increased at 5h after SALI (Figures 1H, S1I and S1J). Thus, we determined that Roquin-1 was expressed mainly in monocyte-derived møs, increased at 5h and decreased at 7h in mice with SALI.

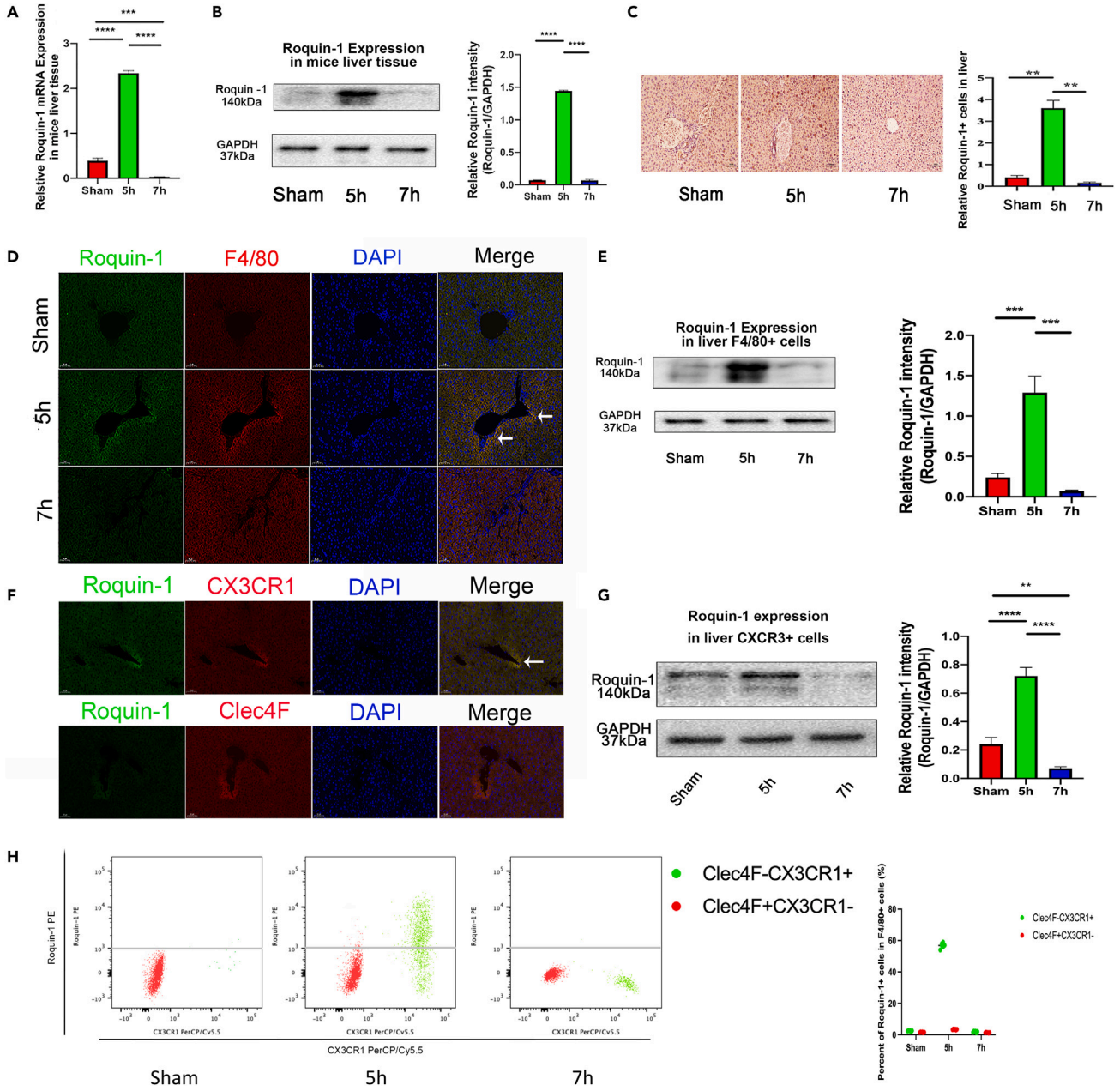

Figure 1. Roquin-1 in liver møs was inhibited and correlated with SALI in WT mice

(A) RT−qPCR analysis of Roquin-1 in mice liver tissue with SALI (n = 6).

(B) WB and quantitation of Roquin-1 expression in mice liver tissue with SALI (n = 6).

(C) IHC stains and quantitation of Roquin-1 in mice liver tissue with SALI (n = 6, scale bars 100 μm).

(D) Immunofluorescence images of Roquin-1 (green) and F4/80+ møs (red) i in mice liver tissue with SALI (n = 6, scale bars: 100 μm).

(E) RT−qPCR of Roquin-1 expression in F4/80+ møs of the mice liver with SALI (n = 6).

(F) Double immunofluorescence labeling of Roquin-1 (green) and CX3CR1+/Clec-4F+ cells (red) in mice liver tissue at 5 h after SALI (n = 6, scale bars: 50 μm).

(G) WB analysis (F) of Roquin-1 expression in mice liver F4/80+CX3CR1+ cells at 5 h after SALI (n = 6).

(H) Liver non-parenchymal cells were isolated from Sham and SALI mice. Clec4F-CX3CR + cells (green dots) and Clec4F + CX3CR-cells (red dots) were gated based on FACS staining of CD11b+F4/80+ cells. Representative Roquin-1 expression of each gated population. $p < 0.01$*, $p < 0.01$ **, $p < 0.001$ ***, $p < 0.0001$ ****. The data are expressed as the mean ± SD. Student's *t* test and one-way analysis of variance (ANOVA) were used to compare two groups and multiple groups, respectively.

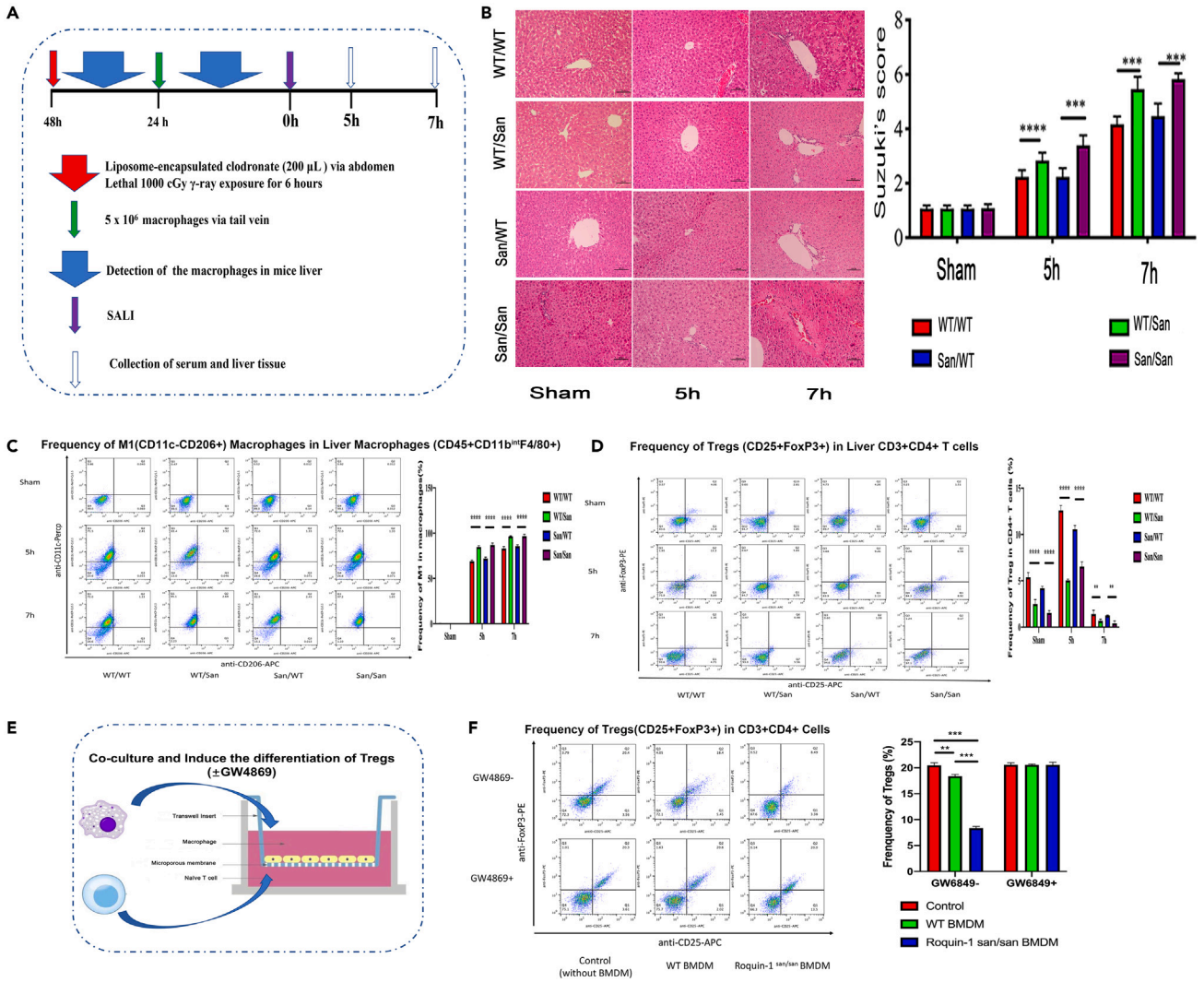

Figure 2. Roquin-1 alleviated SALI by promoting the differentiation of Tregs via MDEVs

(A) Schematic overview of experiments analyzing the effect of Roquin-1 in chimeric mice with SALI (n = 6 mice in every group at each observation time).

(B) HE stains (scale bars: 100 μm), Suzuki's score in chimeric mice after SALI.

(C–D) Flow cytometry of M1 møs (C, CD11b+F4/80+CD11C + CD206-) and Tregs (D, $CD3^+CD4^+CD25$+FoxP3) in mouse liver tissue after SALI (n = 6).

(E) The protocol for the coculture of BMDMs and naive T cells.

(F) Flow cytometry analysis of Treg ($CD3^+CD4^+CD25$+FoxP3+) differentiation in the coculture of WT/Roquin-1san/san BMDMs with/without GW4869 (Inhibitor of EVs) (n = 6). $p < 0.01$*, $p < 0.01$ **, $p < 0.001$ ***, $p < 0.0001$ ****. The data are expressed as the mean ± SD. Student's *t* test and ANOVA were used to compare two groups and multiple groups, respectively.

Roquin-1 in macrophage alleviates SALI by decreasing M1-polarization and promoting Treg-differentiation via MDEVs

To determine the function of Roquin-1 in SALI, we performed the chimeras and the SALI model in mice. We constructed the chimera in mice by tail vein injection of WT/Roquin-$1^{san/san}$ bone marrow-derived mø (BMDM) into WT and Roquin-$1^{san/san}$ mice (Figure 2A). The groups were defined as the recipient/donor combinations below: WT/WT, WT/San, San/WT, and San/San. We found that WT/San group and San/San group had higher Suzuki's scores and serum ALT/AST than WT/WT and San/WT groups (Figures 2B and S2A). Meanwhile, we did not observe significant differences between WT/San and San/San groups. These results reveal the protective function of Roquin-1 in møs with SALI.

To determine the mechanism of Roquin-1 in SALI, we used RT-qPCR to test the inflammatory cytokines in mice liver tissues 5 h after SALI. We found that the mRNA expressions of TGF-β, Foxp3, and IL-10 in WT/WT and

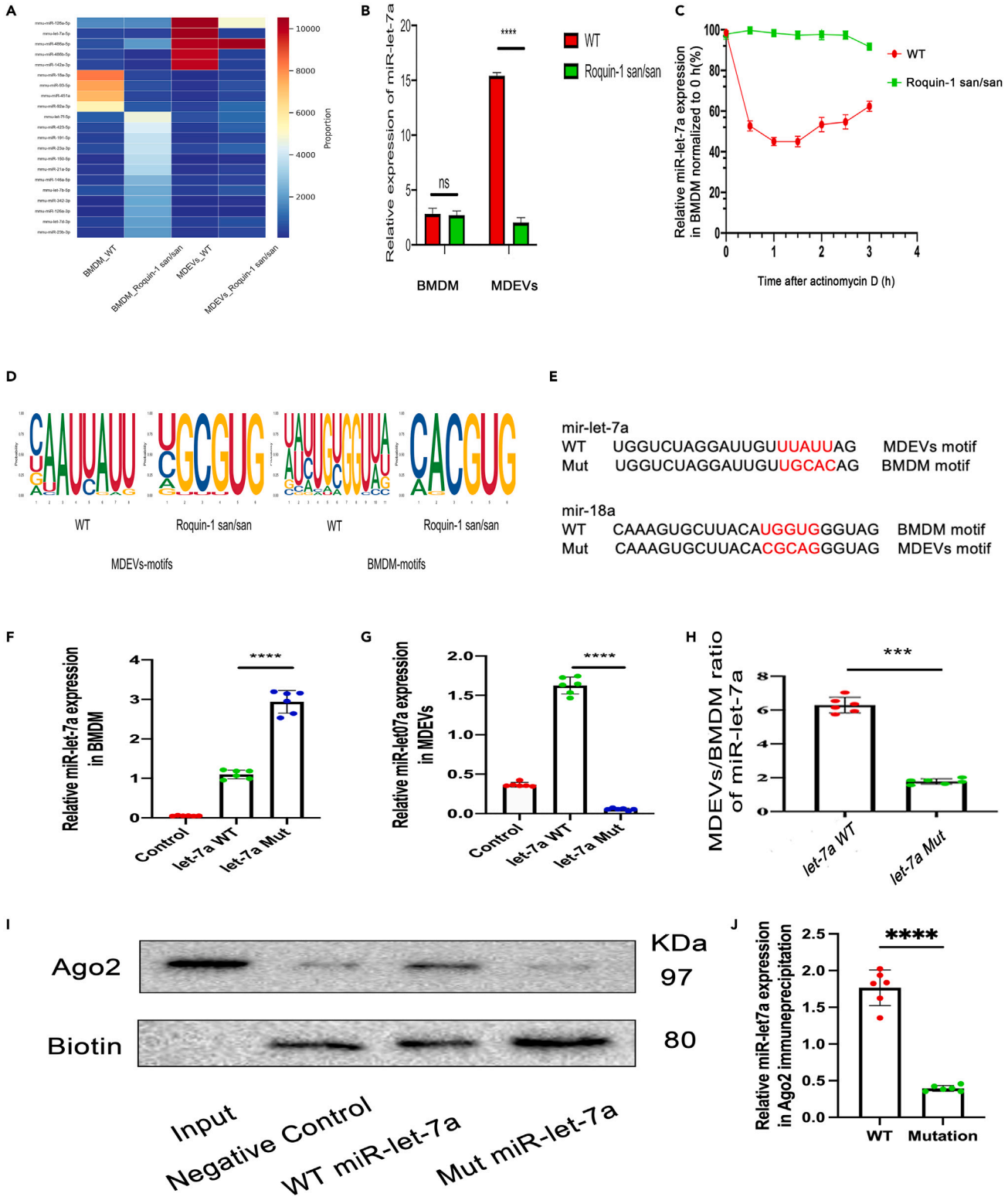

Figure 3. Roquin-1 modulated the sorting of miRNAs into MDEVs by specific miRNAs-motif and Ago2 involved in it

(A) Heatmap of miRNAs in BMDM and MDEVs by miRNA sequencing analysis (n = 6).

(B) RT–qPCR shows the relative expression levels of mature miR-let-7a in BMDM/MDEVs normalized to U6 (n = 6).

(C) The relative expression of miR-let-7a in WT and Roquin-1san/san BMDM treated with actinomycin.

Figure 3. *Continued*

(D) Unbiased analyses of specific miRNA motifs in BMDM and MDEVs.

(E) The miR-let-7a-BMDM-miRNA motif (top) and miR-18a-MDEV-miRNA motif (bottom).

(F and G) The miR-let-7a WT and mut were constructed in BMDM. RT−qPCR was used to detect miR-let-7a expression in miR-let-7a WT/mut BMDM and MDEVs (n = 6).

(H) The MDEVs/BMDM ratio of miR-let-7a (WT) and miR-let-7a (mutation) (n = 6).

(I) WB of WT/Mut miR-let-7a pulldown in BMDM.

(J) The miR-let-7a WT and mut were constructed in BMDM. RT−qPCR was used to detect miR-let-7a expression in Ago2 immunoprecipitation (n = 6).

$p < 0.01$*, $p < 0.01$ **, $p < 0.001$ ***, $p < 0.0001$ ****. The data are expressed as the mean ± SD. Student's *t* test and ANOVA were used to compare two groups and multiple groups, respectively.

San/WT groups were prominently higher than those in WT/San and San/San groups. However, compared with WT/San and San/San groups, IL-6 and TNF-α in WT/WT and San/WT groups were significantly decreased (Figure S2B). Moreover, we observed that the frequencies of Tregs in WT/WT and San/WT groups were significantly upregulated than in WT/San and San/San groups, and the frequencies of M1 møs showed the opposite changes (Figures 2C and 2D). Meanwhile, the IL-6, IL-10, TNFα and TGF-β in serum showed similar changes as the RT-qPCR and flow cytometer (Figure S2C). These results indicated that Roquin-1 in møs reduced the ratio of M1 møs and upregulated the frequency of Tregs in mice.

Additionally, by the slope of the correlation curve between møs and Tregs (Figure S2D), we hypothesized that Roquin-$1^{san/san}$ møs might decrease the frequencies of Tregs more effectively than WT møs. To verify the function and mechanism of mø-specific Roquin-1in the frequencies of Tregs, we constructed the coculture system of BMDM and naive T cells and induced Tregs differentiation *in vitro*. Meanwhile, GW4869, which inhibited the release of MDEVs, was used to examine the function of MDEVs (Figure 2E). According to flow cytometry in T cells (Figure 2F) and ELISA in the supernatant (Figure S2E), we found that Roquin-1in BMDM upregulated the differentiation of Tregs, while GW4869 could remove the affection of Roquin-1 in Tregs differentiation. Then, to exclude the possibility that MDEVs regulates the suppressive function of Tregs, we performed the coculture of $CD3^+CD25^-$ T cells and Tregs and used flow cytometry to detect $CD3^+CD25^-$ T cell proliferation. We found that both WT MDEVs and Roquin-$1^{san/san}$ MDEVs could not affect the suppressive activity of Tregs on $CD3^+CD25^-$ T cells (Figure S2F). These results revealed that Roquin-1 in mø promoted the differentiation of Tregs via MDEVs.

Roquin-1 in BMDM regulates miRNA sorting in MDEVs by specific miRNA motifs

Previous studies have shown that EVs were transporters of mRNA, miRNA, cytokines, proteins, enzymes, molecular chaperones, and signal molecules. Therefore, we isolated MDEVs from WT and Roquin-$1^{san/san}$ BMDM (Figures S3A and S2B) and evaluated the size, secretion rate, and small RNA concentration of MDEVs (Figures S3C–S3E). We found that Roquin-1 could not affect the size/secretion rate of MDEVs and miRNA concentration in MDEVs. According to the aforementioned results, we hypothesized that Roquin-1 modulated the miRNAs sorting in MDEVs. To verify our assumption, we performed the miRNAs sequencing assays in BMDM and MDEVs. The results showed that miRNAs in BMDM were not the same as those in MDEVs (Figure 3A). MiR-let-7a and miR-18a showed the most significant changes below: Compared with WT groups, miR-let-7a in Roquin-$1^{san/san}$ MDEVs decreased significantly, and miR-18a was unchanged. In contrast, miR-let-7a in Roquin-$1^{san/san}$ BMDM did not change significantly, and miR-18a decreased significantly. Meanwhile, the RT-qPCR showed the same changes as the miRNA-sequence analysis (Figures 3B and S3F).

To reveal the mechanism by which Roquin-1 affected miRNA accumulation in BMDM, the primary miR-let-7a and miR-18a in BMDM were detected (Figures S3G and S3H). We found no significant difference in primary miR-let-7a and miR-18a between WT and Roquin-$1^{san/san}$ BMDM. Meanwhile, to exclude the possibility of false-negative, we used three different primers to specifically amplify miR-let-7a in BMDM and miR-18a in MDEVs (Figures S3I and S3J). The results showed no significant differences between WT BMDM/and Roquin-$1^{san/san}$ BMDM in miR-let-7a, while miR-18a in WT and Roquin-$1^{san/san}$ MDEVs showed the same results.

Then, we used actinomycin D[3] to inhibit miR-let-7a and miR-18a decay. At 3 h after treatment, miR-let-7a in WT BMDM was significantly lower than in Roquin-$1^{san/san}$ BMDM (Figure 3C). Meanwhile, GW4869 could eliminate the difference between WT and Roquin-$1^{san/san}$ BMDM (Figure S3K). Conversely, miR-18a in Roquin-$1^{san/san}$ BMDM was significantly lower than in WT BMDM, and GW4869 could not eliminate the significant difference (Figures S3L and S3M). These results demonstrate that Roquin-1 modulates the selected miRNA sorting in MDEVs instead of affecting miRNA production and decomposition in BMDM.

Furthermore, by the unbiased search for specific motifs of miRNAs sequencing assay in BMDM and MDEVs, we detected different motifs significantly over-represented in MDEVs-miRNAs and BMDM-miRNAs, respectively (Figure 3D). Then, we cloned MDEVs-miRNA miR-let-7a and BMDM-miRNA miR-18a and converted the miR-let-7a motif of MDEVs-miRNAs to it of BMDM-miRNA and changed miR-18a into MDEVs motif (Figure 3E). Furthermore, we construct the endogenous expression of miR-let-7a WT and mutation in BMDM and use RT-qPCR to detect miR-let-7a expression in BMDM and MDEVs. We found that miR-let-7a in BMDM with mutation miR-let-7a increased significantly (Figure 3F), while miR-let-7a in MDEVs with WT miR-let-7a was considerably higher than it in miR-let-7a mutation MDEVs (Figure 3G). Meanwhile, the same method was used to build miR-18a WT and mutation BMDM. Compared to miR-let-7a, the results showed the reverse differences in miR-18a (Figures S3N and S3O). Additionally, according to the sequence data, miR-18a had a lower MDEVs/BMDM ratio than miR-let-7a, miR-486a and miR-142a (Figure S3P). However, converting the miR-let-7a MDEVs-miRNAs motif to the BMDM-miRNAs motif resulted in a lower MDEVs/BMDM ratio (Figure 3H), and the conversion of MDEVs-miRNAs motif to the BMDM-miRNAs motif in miR-18a could upregulate the MDEVs/BMDM ratio significantly (Figure S3Q). Therefore, the aforementioned results determine that the specific motifs of miRNAs in BMDM determine the miRNAs sorting in MDEVs.

Based on the aforementioned evidence, we postulated that EXO- and CELL-motifs interact with specific miRNA-binding proteins as part of a process for sorting. A previous study showed that Ago2, a component of RNA-induced silencing complex, is involved in the miRNA sorting in EVs.[24] To investigate this, we performed pull-down assays utilizing cell lysates treated with biotinylated miR-let-7a or miR-18a, either in their native form or the mutation form, demonstrating the most significant EVs enrichment among the several motifs observed. The proteins bound to the different miRNAs were then analyzed by WB. We found that Ago2 bind with WT and mut miR-18a instead of mut miR-let-7a and WT miR-18a (Figures 3I and S3K). Meanwhile, we built the mutation miR-let-7a/miR-18a in BMDM and performed the Ago2-immunoprecipitation in WT and mutation miR-let-7a/miR-18a BMDM. The RT-qPCR showed that the binding of WT miR-let-7a to Ago2 was significantly higher than that of mut miR-let-7a, while miR-18a showed the opposite change (Figures 3J and S3S).

According to the aforementioned results, we determined that Roquin-1 in BMDM modulated the selected miRNA sorting in MDEVs by the specific miRNA motif, and Ago2 might involve in it by its binding with the specific miRNA motif.

Roquin-1 in BMDM promotes Ago2 localization in MVE and secretion to MDEVs

Previous studies revealed that Ago2 is essential in microvesicle (MVE) and MDEV formation.[25] The confocal immunofluorescence found increased Ago2-CD63 (MVE marker) colocalization in WT BMDM than in Roquin-1$^{san/san}$ BMDM. Compared with WT BMDM, Ago2 colocalization with DCP1a (P-body marker) increased in Roquin-1$^{san/san}$ BMDM. Meanwhile, colocalization of CD63 and DCP1a was seldom observed. In contrast, DCP1a-positive fractions are always colocalized with Ago2 in Roquin-1$^{san/san}$ BMDM (Figures 4A and S4A–S4C).

To verify the aforementioned result, we used ultracentrifugation to isolate subcellular fractionations (P-body and MVE), adjusted the total protein concentration to 1 μg/ml, and detected Ago2 expression in the same volume of subcellular fractionations. Roquin-1 did not affect Ago2 fractionation with P-body markers (DCP1a and GW182). However, more Ago2 was present in MVE markers (Rab7 and Flot1) from WT BMDM than Roquin-1$^{san/san}$ BMDM (Figures 4B and 4C). Meanwhile, Ago2 fractionation with MVE in Roquin-1$^{san/san}$ BMDM was significantly less than in WT BMDM (Figure S4D). Then, transmission electron microscopy and NanoSight analysis showed that Roquin-1 did not regulate typical size profiles for MDEVs and MVE (Figures S4E–S4G).

Furthermore, we compared equal numbers of MDEVs by WB and used HSP70 as the loading control. We found an increase in Ago2 and GW182 in WT MDEVs compared to Roquin-1$^{san/san}$ MDEVs (Figure 4D). Similarly, Ago2 in WT MDEVs was significantly higher than Ago2 in Roquin-1$^{san/san}$ MDEVs (Figure 4E). Meanwhile, the difference in Dicer between WT MDEVs and Roquin-1$^{san/san}$ MDEVs was not observed (Figure 4D). DCP1a (P-body marker) was undetectable in MDEVs, in accord with its lack of colocalization with MVE (Figure 4D). Dicer and GW182 were undetectable in MVE purified from WT and Roquin-1$^{san/san}$ BMDM (Figure 4D).

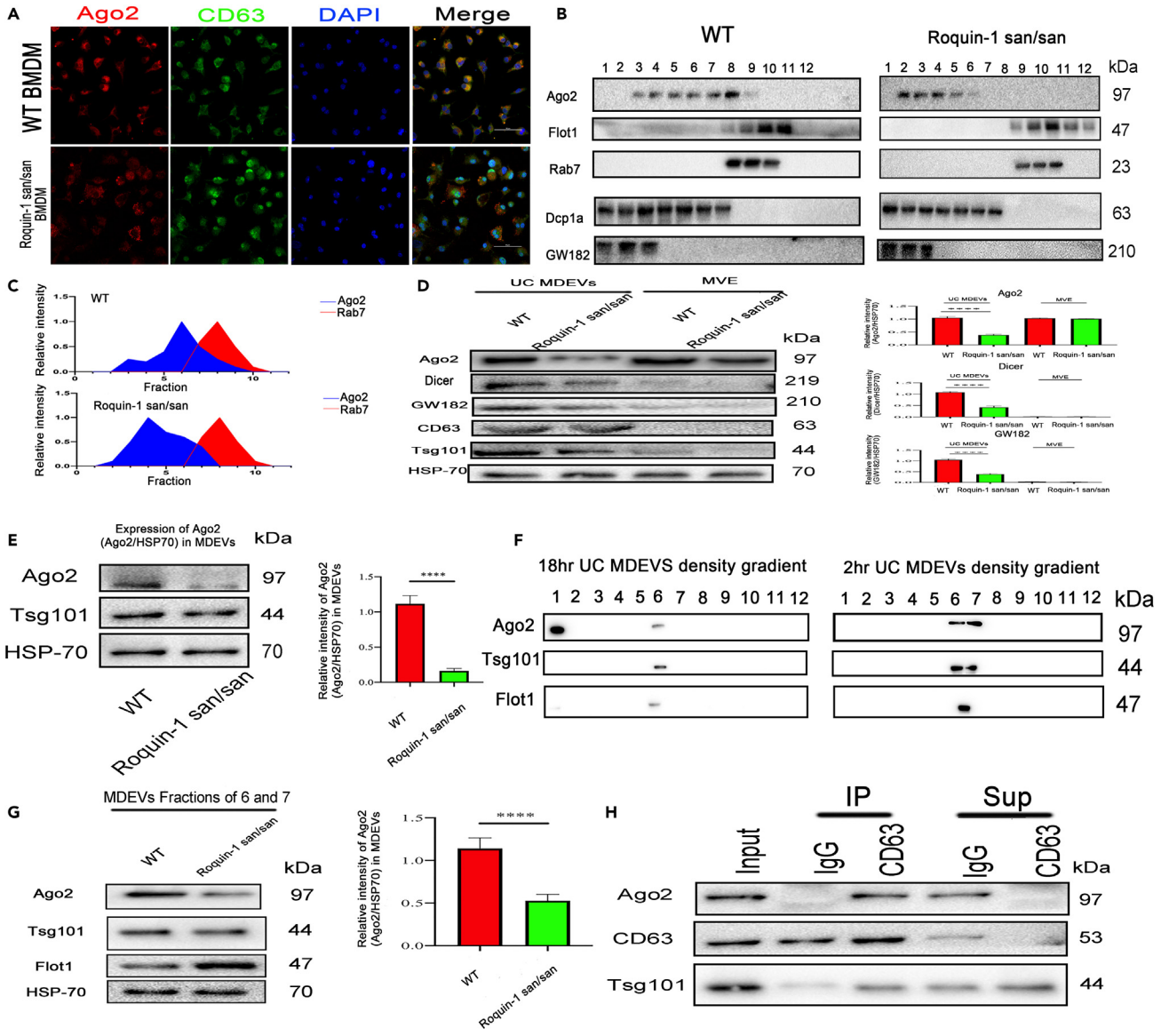

Figure 4. Roquin-1 regulated Ago2 localization to MVEs in BMDM and secretion to MDEVs

(A) Representative confocal immunofluorescence images of Ago2 and CD63 in WT and Roquin-1san/san BMDM (n = 6, scale bars: 20 μm).

(B) WB of WT and Roquin-1san/san BMDM subcellular fractionations through the continuous iodixanol gradient for Ago2, MVE marker (Flot1 and Rab7), and P-body marker (DCP1a and GW182) (n = 6).

(C) The relative intensities of Ago2 and Rab7 in the WT and Roquin-1san/san fractions (n = 6).

(D) WB (K) and quantification in equal numbers of MDEVs and MVE from WT and Roquin-1san/san BMDM. HSP70 was used as the loading control (n = 6).

(E) WB and quantification of Tsg101 in the equal number of MDEVs isolated from WT and Roquin-1san/san BMDM (n = 6). HSP70 was used as the loading control.

(F) WB of Ago2, Flot1 and Tsg101 from iodixanol density gradient fractionation of 18-h and 2-h MDEVs from Roquin-1san/san BMDM (n = 6).

(G) WB and quantification of Ago2, Flot1, and Tsg101 in an equal number of fractions 6 and 7 from iodixanol density purification of 18-h MDEVs (n = 6). HSP70 was used as the loading control.

(H) MDEVs from WT BMDM were IP with an antibody against CD63 or normal mouse IgG and immunoblotted (IB) for the indicated proteins (n = 6). $p < 0.01$*, $p < 0.01$ **, $p < 0.001$ ***, $p < 0.0001$ ****. The data are expressed as the mean ± SD. The Student's *t* test was used for comparison between the two groups.

Since Ago2 could be present in fluids and MDEVs might contain non-vesicle protein, we purified MDEVs by density gradient centrifugation, adjusted the total protein concentration to 1 μg/ml, and detected protein expressions in the same volume of MDEVs. We found the co-fractionation of Ago2 and EVs-markers at the selected EVs density. The result showed protein aggregates corresponding to Ago2 in denser bits and soluble proteins corresponding to lighter fractions (Figure 4F). Then, compared with equal numbers of WT

MDEVs, Ago2 in Roquin-1$^{san/san}$ MDEVs was significantly lower (HSP-70 as loading control) (Figure 4G). Furthermore, to demonstrate Ago2 association with MDEVs, WT MDEVs were immunoprecipitated with anti-CD63 antibody. MDEVs from BMDM were immunoprecipitated with an antibody against CD63 or normal mouse IgG and immunoblotted for the indicated proteins. Input is 20% of the sample used in the immunoprecipitation. The supernatant is 20% of the volume on top of the beads after immunoprecipitation and before washing. We found that Ago2 could be coprecipitated and depleted from the supernatant by the anti-CD63 antibody instead of the immunoglobulin G antibody (Figure 4H).

Additionally, we performed the dot-blot assay to determine the location of Ago2 in MDEVs. We performed the immunoblot and used Tween 20 to permeabilize MDEVs. In accord with Ago2 being an internal EVs cargo, Ago2 was observed in the presence of Tween 20 (Figure S4H). These aforementioned results demonstrated that Roquin-1 in BMDM promoted the localization of Ago2 in MVE and the secretion of Ago2 in MDEVs.

Roquin-1 in BMDM promotes Ago2-K258 ubiquitination and inhibits Ago2-S387 phosphorylation

A previous study has shown that the secretion of Ago2 into EVs was regulated by the Ago2 phosphorylation.[26] We found that Roquin-1 in BMDM inhibited Ago2 S387-phosphorylation (Figure S5A). Meanwhile, we performed the co-immunoprecipitation and immunofluorescence to demonstrate that Roquin-1 connects with Ago2 directly (Figures 5A and 5B).

Furthermore, previous studies have determined that Roquin-1 could bind with its target protein and increase its ubiquitination.[11] Thus, we assumed that Roquin-1 upregulated Ago2-ubiquitination and inhibited Ago2-S387-phosphorylation. To assess the function of Roquin-1 in Ago2-phosphorylation, we used the Roquin-1$^{133-1330}$ mutation, which lost ubiquitination activity, to construct Roquin-1$^{133-1330}$ endogenous expression in BMDM. Compared with WT Roquin-1, Roquin-1$^{133-1330}$ decreased Ago2 ubiquitination and increased Ago2-S387-phosphorylation (Figure 5C). Then, we used the SWISS database to speculate on the ubiquitination sites of Ago2 (Figure 5D) and constructed the Ago2-K258 mutant plasmid to build the endogenous expression of Ago2-K258 mutation (Ago2 KR) in BMDM. The results showed that the phosphorylation of Ago2-WT in BMDM is significantly lower than in Ago2-KR (Figure 5E). Moreover, we found that the ubiquitination of Ago2 WT was considerably higher than that of Ago2 KR. At the same time, decreased Roquin-1 inhibited Ago2-WT ubiquitination but did not affect the Ago2-KR ubiquitination (Figure 5F). Additionally, we evaluated the function of Ago2-KR mutation and Roquin-1$^{133-1330}$ mutation on the Ago2-location in P-body and MVE. We found that both the Roquin-1$^{133-1330}$ mutation and the Ago2-K258 mutation increased the Ago2 location in P-body and decreased the Ago2 location in MVE (Figure S5B). The aforementioned results indicated that Roquin-1 in BMDM inhibited Ago2-S387- phosphorylation by upregulating Ago2-K258 ubiquitination and increased Ago2 location in MVE.

Ago2 affects the miRNAs sorting in MDEVs by particular miRNAs motif and Ago2-S828 phosphorylation

To demonstrate the function of Roquin-1 and Ago2 in the selected miRNAs sorting in MDEVs, we used fluorescent-label selected miRNAs to assess the colocalization with Ago2 and MVE in BMDM. Roquin-1 promoted the colocalization of Ago2 and miR-let-7a (Figure 5G) and the location of miR-let-7a in MVE (Figure 5H). Meanwhile, Roquin-1$^{san/san}$ upregulated the colocalization of Ago2 and miR-18a (Figure S5C). In comparison, Roquin-1 did not affect the miR-18a location in MVE (Figure S5D). These results revealed that Roquin-1 modulated the site of selected miRNAs in Ago2 and MVE.

Furthermore, we constructed S387E (mCherry-Ago2 constructs containing phosphomimetic) and S387A (phospho-resistant mutation) and found that Ago2-S387 phosphorylation could not regulate the colocalization of Ago2 and selected miRNAs (Figures S5E and S5F). We assumed there might be another phosphorylation site to modulate the bind between Ago2 and selected miRNAs. Therefore, we performed the mass spectrum of Ago2 in the WT and Roquin-1$^{san/san}$ BMDM. We found that Roquin-1 upregulated the phosphorylation of Ago2 at S387 and S828 sites simultaneously (Figure S5G). To test whether Ago2-S828 phosphorylation regulates the miRNAs sorting in MDEVs, we built the S828-Phosphorylation mutant of Ago2 in BMDM (Figure S5H). We found that the S828-Phosphorylation of Ago2 could not affect the secretion of MDEVs or MVE (Figure S5I) and the small RNA content in MDEVs or MVE (Figure S5J). To identify the selective change of miRNAs in MDEVs, we adjusted the same concentration of miRNAs in each sample and performed RT-qPCR. Compared

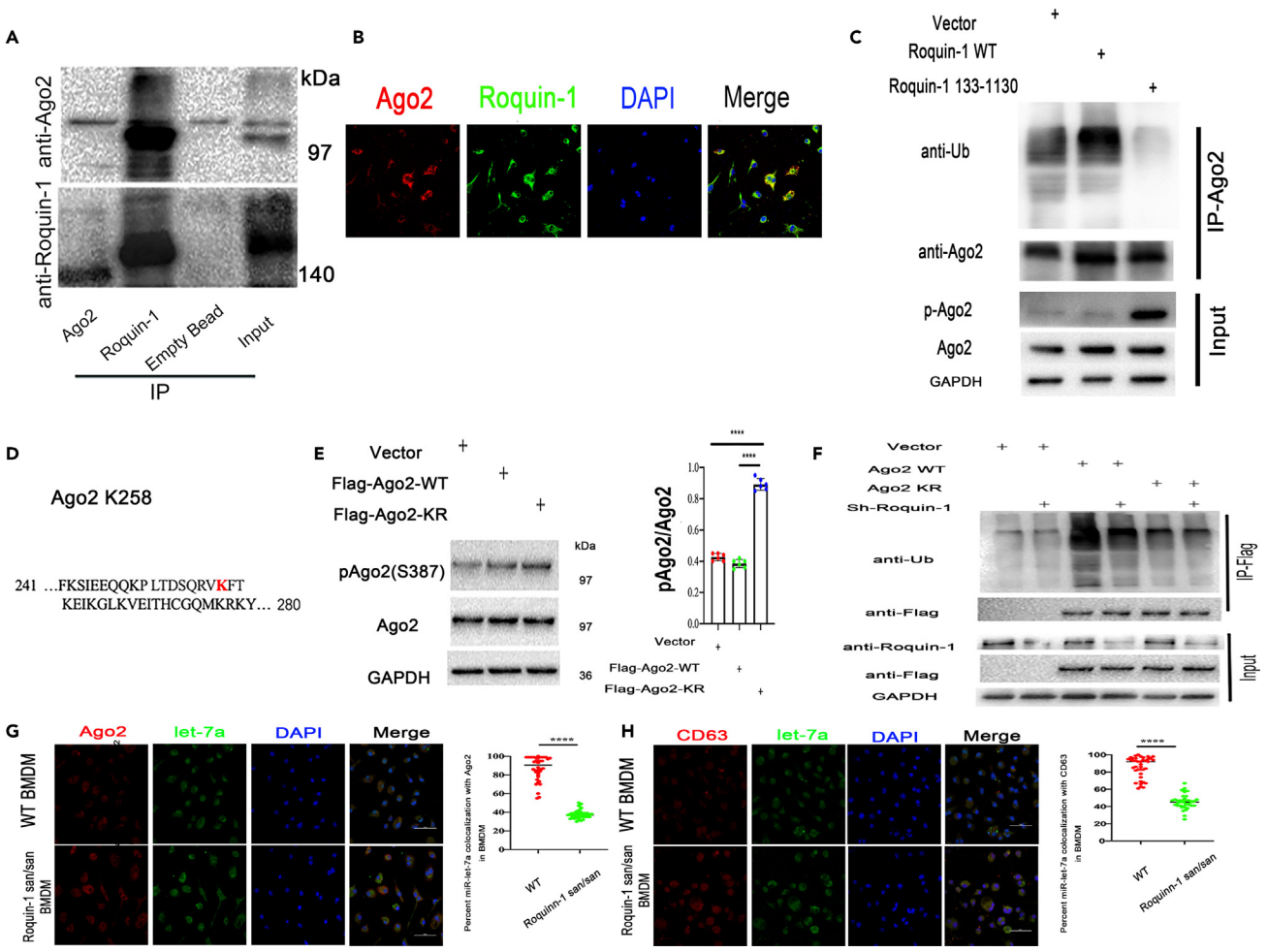

Figure 5. Roquin-1 regulated Ago2 sorting in MDEVs by upregulating ubiquitination and inhibiting S387/S828 phosphorylation in BMDMs simultaneously

(A) WB of the coimmunoprecipitation of Roquin-1 and Ago2 in BMDM (n = 6).

(B) Immunofluorescent labeling of Roquin-1 (green) and Ago2 (red) in BMDM (n = 6, scale bars: 20 μm).

(C) Roquin-1 133–1330, which was deleted from the RING domain and lacked ubiquitination activity, was used to investigate the relationship between Roquin-1 ubiquitination activity and the phosphorylation of Ago2 in BMDM (n = 6).

(D) The candidate ubiquitin sites on Ago2.

(E) The expression of Ago2 WT and KR mutant ubiquitination was compared using si-Roquin-1 to interfere with its expression and coprecipitate FLAG (n = 6).

(F) The relationship between mutations in the ubiquitination sites of Ago2 KR and the phosphorylation of Ago2 (n = 6).

(G) The co-localization of Ago2 and miR-let-7a in WT/Roquin-1san/san BMDM (n = 6).

(H) The co-localization of miR-let-7a and CD63 in WT/Roquin-1san/san BMDM (n = 6). $p < 0.01$*, $p < 0.01$ **, $p < 0.001$ ***, $p < 0.0001$ ****. The data are expressed as the mean ± SD. Co-localization Student's *t* test was used for comparison between the two groups.

with the WT group, miR-let-7a in Ago2-S828-Phosphorylation mutant MDEVs increased significantly while miR-18a reduced (Figure S5K). Then, we found that the Ago2-S828 mutant promoted the colocalization of Ago2 and miR-let-7a and inhibited the colocalization of Ago2 and miR-18a (Figures S5L and S5M). Meanwhile, we performed RNA Binding Protein Immunoprecipitation of Ago2-WT/Ago2 S828-Phosphorylation mutant and used RT-qPCR to detect miR-let-7a and miR-18a in Ago2-WT and Ago2 S828-Phosphorylation mutant immunoprecipitation. The result showed that miR-18a, but not miR-let-7a, was amplified from Ago2 WT immunoprecipitation (Figure S5N). Additionally, we built the miR-let-7a/miR-18a special motif mutation in BMDM and used RIP of Ago2-WT and RT-qPCR to detect the colocation between Ago2 and miR-let-7a/miR-18a. We found that the miR-let-7a mutation decreased its colocation with Ago2, while the miR-18a mutation increased its colocation with Ago2 (Figure S5O). These data indicated that Ago2-S828-Phosphorylation modulated its colocation to the specific motif of selected miRNAs.

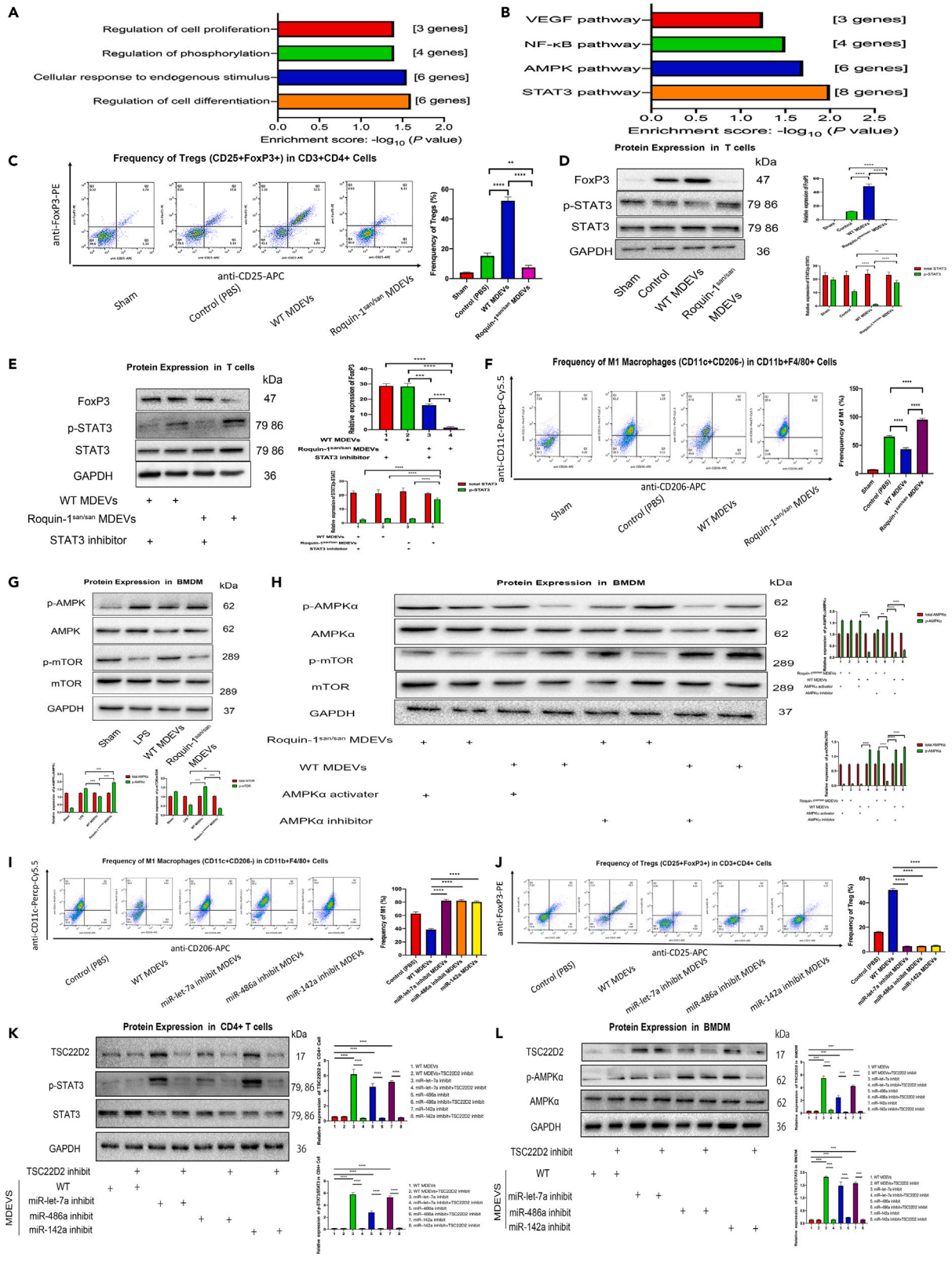
A
Regulation of cell proliferation
Regulation of phosphorylation
Cellular response to endogenous stimulus
Regulation of cell differentiation
[3 genes]
[4 genes]
[6 genes]
[6 genes]
Enrichment score: -log10 (P value)
B
VEGF pathway
NF-κB pathway
AMPK pathway
STAT3 pathway
[3 genes]
[4 genes]
[6 genes]
[8 genes]
Enrichment score: -log10 (P value)
C
Frequency of Tregs (CD25+FoxP3+) in CD3+CD4+ Cells
anti-FoxP3-PE
anti-CD25-APC
Sham
Control (PBS)
WT MDEVs
Roquin-1san/san MDEVs
Frenquency of Tregs (%)
D
Protein Expression in T cells
kDa
FoxP3
p-STAT3
STAT3
GAPDH
47
79 86
79 86
36
Sham
Control
WT MDEVs
Roquin-1san/san MDEVs
E
Protein Expression in T cells
kDa
FoxP3
p-STAT3
STAT3
GAPDH
47
79 86
79 86
36
WT MDEVs
Roquin-1san/san MDEVs
STAT3 inhibitor
Relative expression of FoxP3
Relative expression of STAT3p-STAT3
total STAT3
p-STAT3
F
Frequency of M1 Macrophages (CD11c+CD206-) in CD11b+F4/80+ Cells
anti-CD11c-Percp-Cy5.5
anti-CD206-APC
Sham
Control (PBS)
WT MDEVs
Roquin-1san/san MDEVs
Frenquency of M1 (%)
G
Protein Expression in BMDM
kDa
p-AMPK
AMPK
p-mTOR
mTOR
GAPDH
62
62
289
289
37
Sham
LPS
WT MDEVs
Roquin-1san/san MDEVs
total AMPKα
p-AMPKα
total mTOR
p-mTOR
H
Protein Expression in BMDM
kDa
p-AMPKα
AMPKα
p-mTOR
mTOR
GAPDH
62
62
289
289
37
Roquin-1san/san MDEVs
WT MDEVs
AMPKα activater
AMPKα inhibitor
I
Frequency of M1 Macrophages (CD11c+CD206-) in CD11b+F4/80+ Cells
anti-CD11c-Percp-Cy5.5
anti-CD206-APC
Control (PBS)
WT MDEVs
miR-let-7a inhibit MDEVs
miR-486a inhibit MDEVs
miR-142a inhibit MDEVs
Frequency of M1 (%)
J
Frequency of Tregs (CD25+FoxP3+) in CD3+CD4+ Cells
anti-FoxP3-PE
anti-CD25-APC
Control (PBS)
WT MDEVs
miR-let-7a inhibit MDEVs
miR-486a inhibit MDEVs
miR-142a inhibit MDEVs
Frequency of Treg (%)
K
Protein Expression in CD4+ T cells
kDa
TSC22D2
p-STAT3
STAT3
GAPDH
17
79, 86
79, 86
36
TSC22D2 inhibit
MDEVS
WT
miR-let-7a inhibit
miR-486a inhibit
miR-142a inhibit
1. WT MDEVs
2. WT MDEVs+TSC22D2 inhibit
3. miR-let-7a inhibit
4. miR-let-7a inhibit+TSC22D2 inhibit
5. miR-486a inhibit
6. miR-486a inhibit+TSC22D2 inhibit
7. miR-142a inhibit
8. miR-142a inhibit+TSC22D2 inhibit
L
Protein Expression in BMDM
kDa
TSC22D2
p-AMPKα
AMPKα
GAPDH
17
62
62
36
TSC22D2 inhibit
MDEVS
WT
miR-let-7a inhibit
miR-486a inhibit
miR-142a inhibit

Figure 6. MDEVs affected Treg differentiation via TSC22D2-STAT3/FoxP3 pathway and regulated M1 polarization via the TSC22D2-AMPKα/mTOR pathway

(A and B) Sequence-based gene expression profile analyses identify the function and/or signaling pathways.
(C) The flow cytometer and quantitation of Tregs in the coculture of WT/Roquinn-1 san/san MDEVs and naive T cells with the inducement of Tregs differentiation (n = 6).
(D) Western blot and quantitation of FoxP3/p-STAT3/STAT3 in Tregs with MDEVs stimulation (n = 6).
(E) Western blot and quantitation of FoxP3/p-STAT3/STAT3 in Tregs with/without the stimulation of MDEVs and/or STAT3 inhibitor (n = 6).
(F) The flow cytometer and quantitation of M1 mø in the coculture of MDEVs and mø with LPS stimulation (n = 6).
(G) Western blot and quantitation of AMPKα/mTOR in BMDM with/without the stimulation of LPS and MDEVs (n = 6).
(H) Western blot and quantitation of AMPKα/mTOR in BMDM with/without the stimulation of MDEVs and/or AMPKα activator/inhibitor (n = 6).
(I) The flow cytometry of M1 mø in the coculture of mø and WT/miR-let-7a/miR-486a/miR-142a inhibit MDEVs with LPS stimution (n = 6).
(J) The flow cytometry of Treg in the coculture of WT/miR-let-7a/miR-486a/miR-142a inhibit MDEVs and naive T cells with the inducement of Tregs differentiation (n = 6).
(K) Western and quantitation of TSC22D2 and p-STAT3 in Tregs with with TSC22D2 inhibit and WT/miR-let-7a/miR-486a/miR-142a inhibit MDEVs (n = 6).
(L) Western and quantitation of TSC22D2 and *p*-AMPKα in BMDM with with TSC22D2 inhibit and WT/miR-let-7a/miR-486a/miR-142a inhibit MDEVs (n = 6).
$p < 0.01$*, $p < 0.01$ **, $p < 0.001$ ***, $p < 0.0001$ ****. The data are expressed as the mean ± SD. The Student's *t* test was used for comparison between the two groups.

MDEVs upregulate Tregs-differentiation via the TSC22D2-STAT3 pathway and inhibit M1-macrophage polarization by TSC22D2-AMPKα-mTOR signaling

At first, for the function of MDEVs, we stained MDEVs (PKH67, Green) and naive T cells/mø (PKH26, Red) and built the coculture of naive T cells/mø and MDEVs. By the confocal imaging, we found that the absorption of MDEVs in naive T cells/mø was not affected by Roquin-1 (Figures S6A and S6B). Then, according to the miRNA sequence assay in MDEVs, we conducted a miRNA target prediction and GO/KEGG enrichment analysis, which revealed significant alternations in the cell differentiation (Figure 6A) and the most considerable enrichment occurring in the STAT3 signaling pathway (Figure 6B). Then, we constructed the coculture of naive T cells and MDEVs. According to flow cytometry (Figure 6C) and ELISA (Figure S6C), we found that WT MDEVs promoted Tregs differentiation while Roquin-$1^{san/san}$ MDEVs inhibited Tregs differentiation. Meanwhile, WB results showed that WT MDEVs inhibited STAT3-phosphorylation and increased FoxP3 expression. In contrast, Roquin-$1^{san/san}$ MDEVs performed the opposite function (Figure 6D). Furthermore, we used Compound C to inhibit STAT3 activity. We observed that WT MDEVs upregulated the expression of FoxP3 by repressing STAT3 phosphorylation in Tregs (Figure 6E).

Meanwhile, we used MDEVs to stimulate mø and induced M1 polarization with LPS. The flow cytometry (Figure 6F) and ELISA (Figure S6D) showed that WT MDEVs inhibited the polarization of M1 mø. However, our study found that MDEVs had no significant effect on STAT3 (Figure S6E). To explore the potential mechanism of MDEVs in mø, according to the GO/KEGG enrichment analysis, we detect the impact of MDEVs on the AMPKα signal. A previous study showed that AMPKα/mTOR pathway could modulate the mø polarization during cerebral ischemia.[27] In accordance with previous studies, western blotting (Figure 6G) detected a significant decrease in AMPKα-phosphorylation and increased mTOR-phosphorylation in the WT MDEVs group compared to the Roquin-$^{1san/san}$ MDEVs group. Then, to detect the function of MDEVs in the AMPKα/mTOR pathway, we used an AMPKα activator and inhibitor to affect the phosphorylation of AMPKα (Figure 6H). Compared with the WT MDEVs group, AMPKα phosphorylation in the Roquin-$1^{san/san}$ MDEVs group was enhanced, and mTOR phosphorylation was inhibited. When the inhibitor/activator was used, the difference between WT MDEVs and Roquin-$1^{san/san}$ MDEVs in mTOR phosphorylation was insignificant.

These results determined that WT MDEVs upregulated Treg differentiation by inhibiting STAT3 phosphorylation and restrained M1 macrophage polarization via the AMPKα-mTOR pathway.

Selective inhibition of miRNAs in MDEVs increases M1 macrophage polarization and decreases Tregs differentiation

To evaluate if the identified miRNAs have a role in MDEVs-mediated anti-inflammatory communication, we examine how they influence the expression of the inflammatory genes. To do this, we knockdown the characteristic miRNAs (miR-let-7a, miR-486a and miR-142a) from MDEVs by miRNA inhibitors. Intriguingly, diminishment of miR-let-7a, miR-486a and miR-142a in BMDM and naive T cells increased the expression of TNF-α and IL-6 mRNA in mø and decreased the expression of TGF-β and IL-10 mRNA in T cells (Figures S6F and S6G). These results support the predicted function of miR-let-7a, miR-486a and miR-142a in mø and naive T cells as TNF-α, IL-6, TGF-β, and IL-10 adaptor molecules.

Subsequently, we investigated whether the absence of these three miRNAs may affect the inflammatory signaling of MDEVs. MDEVs were extracted from the cell culture media of BMDM modified to downregulate levels of miR-let-7a, miR-486a, miR-142a and a control cell line. The data indicated no significant difference among the three groups in MDEVs size (Figure S6H). In addition, we determined that the number of particles and small RNA volume secreted by control BMDM is equal to that of miR-let-7a/miR-18a knockdown BMDM (Figures S6I and S6J). These findings support the notion that normal control MDEVs and miR-let-7a/miR-486a/miR-142a knockdown MDEVs have structural similarities. Importantly, when stimulated with si-Roquin-1, BMDM generated MDEVs with decreased miR-let-7a, miR-486a and miR-142a. (Figure S6K). Meanwhile, we confirmed that the reduction of specific microRNAs in BMDM transduced with miRNA inhibitors also leads to the depletion of microRNA in MDEVs (Figure S6L). These results reveal the effective modification of MDEVs to remove specific micro-RNA cargo.

Attentionally, MDEVs obtained from BMDMs (WT, Roquin-1$^{san/san}$, miR-let-7a inhibit, miR-486a inhibit, and miR-142a inhibit) were co-cultured with BMDM and naive T cells to assess the effect of selective miRNA deletion on MDEVs anti-inflammatory communication. Using flow cytometry, we found that the absence of miR-let-7a, miR-486a and miR-142a in MDEVs diminished their ability to inhibit mø polarization and upregulate Tregs differentiation (Figures 6I, 6J, S6M, and S6N). These results indicated that this group of miRNAs might regulate mø polarization and Tregs differentiation via MDEVs derived miRNA delivery.

Finally, we used miRDB, TargetScan and StarBase to predict the common Target of the RNAs. The result showed that TSC22D2 was the common target gene of these three miRNAs (Figure S6O). Then, we used RT-qPCR and WB to detect the mechanism of miR-let-7a, miR-486a and miR-142a in mø polarization and Tregs differentiation. The results showed that inhibition of miR-let-7a, miR-486a and miR-142a in MDEVs upregulated TSC22D2 expression and the phosphorylation of STAT3 and AMPKα in mø and Tregs (Figures 6K, 6L, and S6P). Then, to validate the miR-let-7a/miR-486a/miR142a binding locations in the 3′UTR of TSC22D2 (Figure S6Q), we performed a luciferase test in BMDM and T cell. Cells were transfected with pGL3-TSC22D2-3′UTR (wt/mut) luciferase report plasmids with miR-let-7a/miR-486a/miR142a inhibitor, non-specific inhibitor (NSI). There was no change in luciferase activity between BMDM/T cells transfected with TSC22D2-3′UTR-mut and miR-let-7a/miR-486a/miR142a inhibitor and BMDM/CD4+ T cells transfected with TSC22D2-3′UTR-mut and NSI. However, compared to cells transfected with TSC22D2-3′UTR and NSI, the luciferase activity in cells transfected with TSC22D2-3′UTR and miR-let-7a/miR-486a/miR142a inhibitor increased significantly (Figure S6R). Based on these findings, we demonstrated that miR-let-7a/miR-486a/miR142a targeted TSC22D2 mRNA3′UTR in BMDM and CD4$^+$ T cells.

Altogether, our findings indicate that WT MDEVs can transmit anti-inflammatory signals. In addition, our results demonstrate that Roquin-1 in mø creates MDEVs with improved anti-inflammatory miRNA cargo capacity. The anti-inflammatory miRNA in MDEVs repressed TSC22D2 expression and STAT3/AMPKα phosphorylation to modulate mø polarization and Tregs differentiation.

WT MDEVs alleviates SALI in mice by increasing Tregs differentiation and decreasing M1 macrophage polarization simultaneously

To investigate the potential *in vivo* capabilities of MDEVs, we first evaluated their biodistribution by labeling MDEVs with FITC. 6-8-week-old male C57BL/6 mice were injected with FITC-labeled WT MDEVs and Roquin-1$^{san/san}$ MDEVs. Twenty-four hours after the injection, perfused organs were collected and detected by flow cytometry. Most labeled MDEVs were found in the spleen, liver and kidney (Figure S7A). Additionally, we discovered that F4/80+ cells were more efficient than F4/80-cells at absorbing MDEVs (Figure S7B), while MDEVs were taken up efficiently by CD4$^+$ cells as well (Figure S7C). Under all settings, there was no difference in uptake between WT MDEVs and Roquin-1$^{san/san}$ MDEVs. HE stains (Figure 7A) and Suzuki's score (Figure 7B) showed that WT MDEVs alleviated SALI while Roquin-1$^{san/san}$ MDEVs aggravated SALI. The ALT and AST (Figure 7C) in serum also determined that WT MDEVs attenuated SALI while Roquin-1$^{san/san}$ MDEVs increased liver injury. To analyze the function of MDEVs on immune response (mø and Treg) *in vivo*, we examined the frequencies of M1 møs (Figure 7D) and Tregs (Figure 7E) in the liver and the TNF-α/TGF-β/IL-6/IL-10 (Figures 7F–7I) in serum. The injection of WT MDEVs upregulated the frequency of Tregs in the liver and TGF-β/IL10 in serum and decreased the frequency of M1 møs in liver and serum TNF-α/IL-6. Meanwhile, the injection of Roquin-1$^{san/san}$ MDEVs performed the opposite function. These results revealed that WT MDEVs might alleviate SALI by promoting Tregs-differentiation and inhibiting M1 polarization.

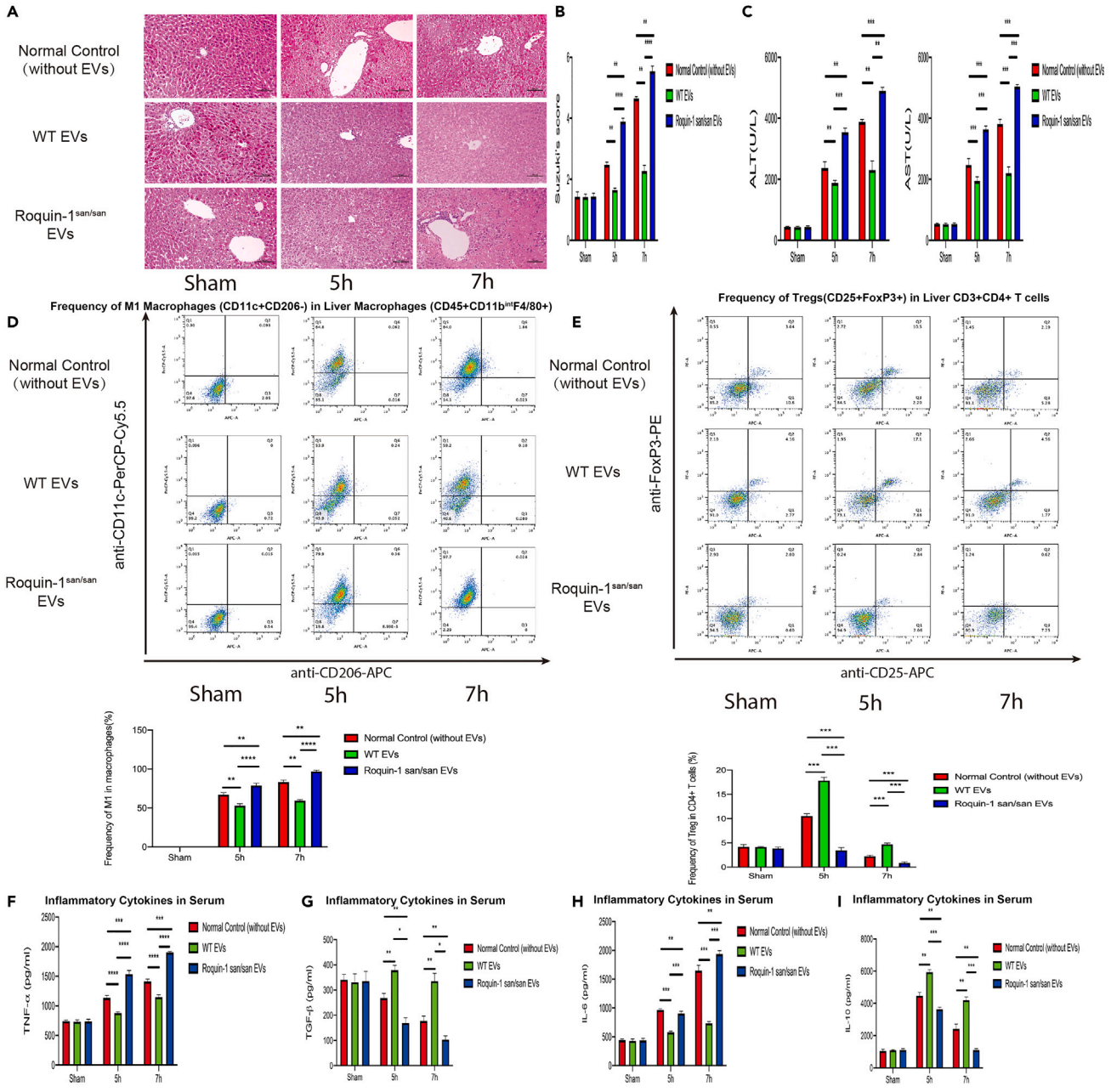

Figure 7. MDEVs alleviate SALI by promoting Tregs differentiation and inhibiting M1 polarization synchronously

(A and B) HE stains (A, scale bars: 100 μm) and Suzuki's score (B) in mice liver during SALI with/without WT/Roquin-1san/san MEDVs injection (n = 6).

(C) serum ALT and AST in SALI mice with/without WT/Roquin-1san/san MEDVs MDEVs injection (n = 6).

(D and E) Flow cytometry and quantitation of M1 møs and Tregs in mice liver during SALI with/without MEDVs injection (n = 6).

(F–I) Serum TNF-α (f)/TGF-β (g)/IL-6 (h)/IL-10 (i) in SALI mice with/without MDEVs injection (n = 6). $p < 0.01$*, $p < 0.01$ **, $p < 0.001$ ***, $p < 0.0001$ ****. The data are expressed as the mean ± SD. The Student's *t* test was used for comparison between the two groups.

Roquin-1 in macrophage is critical to miRNA sorting in MDEVs and inflammatory profile in patients with SALI

Then, we investigated whether these findings apply to SALI patients. At first, we collected SALI patients and used RT-qPCR to examine the expression of Roquin-1 in the liver tissue of SALI patients and healthy persons. A total of 10 patients with SALI and seven healthy persons (normal group) were collected in our study. The inclusion criteria were designed by the Social of Critical Care Medicine Guideline in 2020 and infected

by Gram-negative bacilli (Table S1). According to RT-qPCR in the liver, Roquin-1 expression in SALI patients was lower significantly than in the normal group (Figure 8A). Roquin-1 was mainly expressed in liver CD11b+ cells and inhibited in SALI patients (Figure 8B). Then, the flow cytometry showed that monocyte-derived mø (CD11b+CD14+CCR2+) was the main source of Roquin-1 in human (Figures S8A and S8B). The SALI patients were characterized by an increased pro-inflammatory profile (M1 mø ratio, TNF-α, IL-6) and decreased anti-inflammatory profile (Tregs frequency, TGF-β, IL-10) (Figure 8C). Notably, the expression of Roquin-1 in humans correlated positively with an anti-inflammatory profile and negatively positively with a pro-inflammatory profile (Figure 8D). These data demonstrated a functional significance for Roquin-1 in the liver. They identified a decrease during SALI, accompanied by an enhanced pro-inflammatory profile and a reduced anti-inflammatory profile, as a mechanism for hepatocellular damage in SALI. We hypothesize that this decrease in Roquin-1 expression modulates the immunological response to sepsis via exosome-mediated mechanisms. Consistent with this, higher pro-inflammatory and lower anti-inflammatory factors were seen in SALI patients, indicating an increase in "M1-like" møs and a decrease in Tregs, similar to our SALF mice model.

Furthermore, the expression of several miRNAs in the patient plasma EVs was evaluated. There was a decrease in miR-let-7a, miR-486a and miR-142a (Figure 8E). In addition, decreased miR-let-7a, miR-486a and miR-142a were identified in patients with SALI relative to healthy patients, similar to the observed decreases in these miRNAs in MDEVs (Figure 3A). Meanwhile, miR-18a was unchanged between groups (Figure 8E), indicating that only a subset of miRNAs in EVs are dysregulated in SALI patients. Furthermore, TSC22D2 expression in the liver nonparenchymal cells, the common target of the three decreased miRNAs, increased in patients with SALI (Figure 8G) and was similar to the change *in vitro* model (Figures 7T–7V). This discovery leads us to postulate that there may be deficiencies in selected miRNA loading in patients with SALI, representing a unique mechanism for the progression of SALI.

DISCUSSION

Our study identified that Roquin-1 in møs alleviated immune response during SALI by promoting Tregs differentiation and inhibiting M1 polarization. At first, Roquin-1 in monocyte-derived møs was inhibited and associated with the inflammatory profiles during SALI. Secondly, Roquin-1in møs upregulated Ago2-K258 ubiquitination on and inhibited Ago2-S387/S828 phosphorylation for modulating selected-miRNAs sorting in MDEVs simultaneously. Third, miRNAs in MDEVs (miR-let-7a/miR-486a/miR-142a) upregulated Tregs differentiation via the TSC22D2-STAT3 signal and simultaneously inhibited M1 polarization via the TSC22D2-AMPKα/mTOR pathway.

Bacterial infections were the leading cause of sepsis. In 40% of sepsis patients, Gram-positive bacteria were identified, followed by Gram-negative bacteria at 38% and fungus at 17%.[28] Recently, another epidemiological investigation has identified the most frequently isolated bacteria in sepsis patients globally.[29] Gram-negative bacteria were discovered in two-thirds of patients with culture-proven sepsis, whereas Gram-positive bacteria were identified in fifty percent. Variations in worldwide infection patterns were detected. In Asia, fewer Gram-positive bacteria were discovered to cause sepsis than in other regions of the world. In comparison, Gram-positive bacteria were more widespread in Europe and Northern America. In our study, we collected the patients with intra-abdominal infections. The pathogenic bacterium in our study includes *Escherichia coli* and *Klebsiella pneumonia*. In Asia, previous study showed that *E. coli* and *K. pneumoniae* were the most prevalent bacteria responsible for bloodstream infection.[30] Furthermore, intra-abdominal infection is usually a mixed infection of various intestinal microorganisms, and the primary pathogens are intestinal flora. The most common pathogens in our country are *E. coli*, *K. pneumonia*, and *Enterococcus faecium*.[31] Therefore, to investigate the mechanism of Roquin-1 in SALI, we used the LPS and D-GALN to build the SALI model in mice.

Unlike local infections, sepsis is a systemic and multidimensional change of the immune system. The dramatically enhanced release of chemokines and pathogen-related molecules is caused by the activation of pro- and anti-inflammatory pathways. According to current knowledge, the dysregulated host response to infection results in early pro-inflammatory responses and insufficient anti-inflammatory responses that regulate pathogen clearance efficiency and limit tissue harm.[32] Infections induce an acute phase response in the liver, which is accompanied by metabolic and immunological alterations.[33] Through distinct local immune cell populations that generate immunomodulatory cytokines that stimulate adaptive immunity, the liver regulates the global immune system. Thus, early liver failure is typically linked with various organ

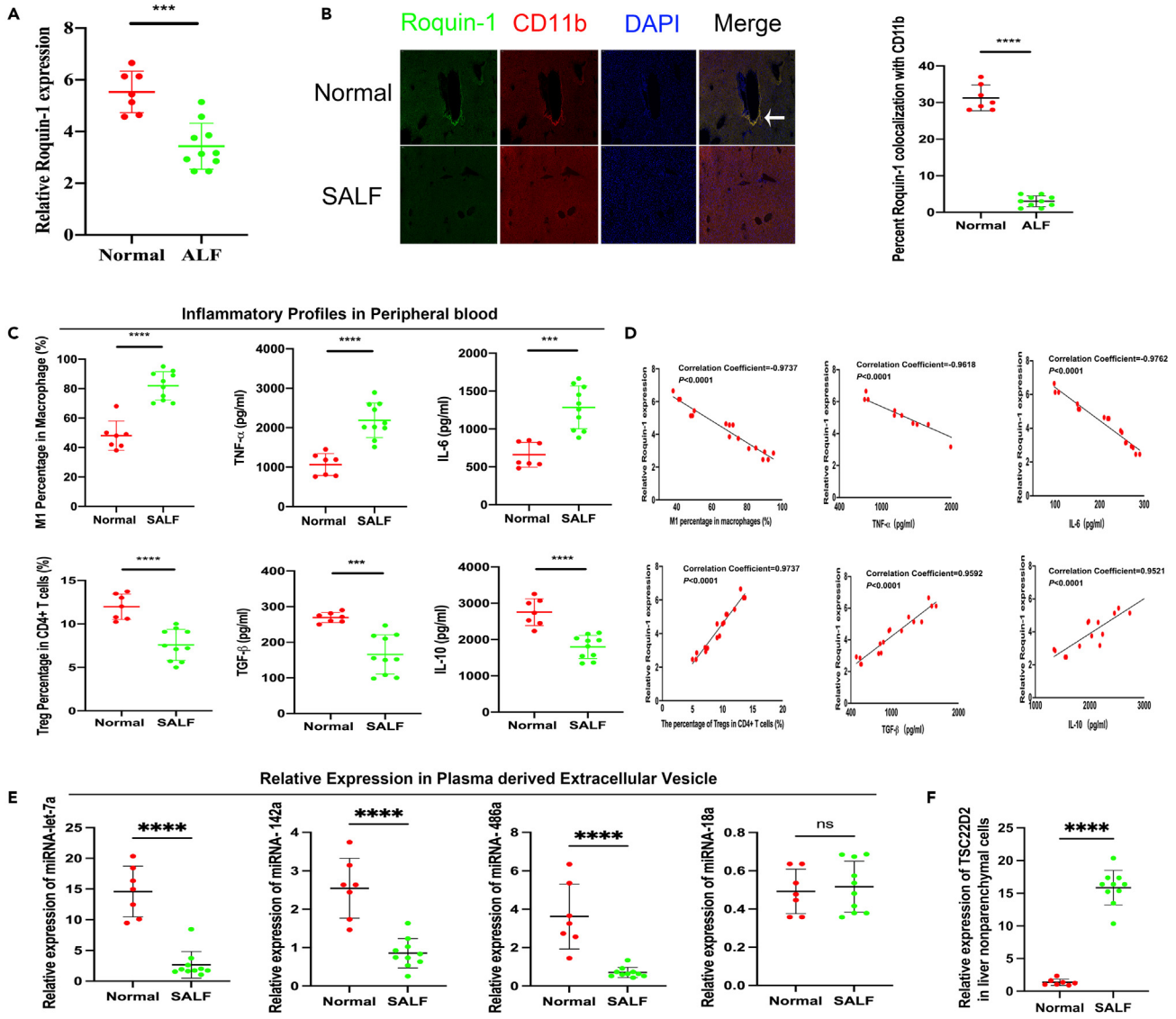

Figure 8. Dysregulation of Roquin-1, inflammatory genes, and miRNA signatures in patients with SALI

(A) Roquin-1 expression in the liver tissue of SALI patients (n = 10 human SALI patients) and control healthy samples (n = 7 healthy controls) was measured by RT−qPCR ($p = 0.002$).

(B) Double immunofluorescence labeling was performed to detect the expression of Roquin-1 (green) in liver CD11b+ møs (red) (normal (n = 7) and SALI (n = 10). Scale bars: 100 μm).

(C) Flow cytometry was performed to assess the frequency of Tregs in $CD4^+$ T cells and the ratio of M1/mø in blood. Serum TGF-β, TNF-α, IL-6 and IL-10 were measured by ELISA.

(D) A regression curve was generated by plotting relative Roquin-1 mRNA expression against TGF-β/TNF-α/IL-6/IL-10/Tregs frequency/M1 ratio in the SALI patient and normal person.

(E) RT-qPCR analysis of miR-let-7a, miR142a, miR-486a and miR-18a in plasma EVs of SALI patients.

(F) RT-qPCR analysis of TSC22D2 in liver of SALI patients. $p < 0.01$*, $p < 0.01$ **, $p < 0.001$ ***, $p < 0.0001$ ****. The data are expressed as the mean ± SD. The Student's *t* test was used for comparison between the two groups.

dysfunction syndromes and a bad prognosis.[34] Liver injury disrupts distant organ function and severely impacts whole-body and tissue metabolism, and it may cause organ failure in the brain, heart, lungs, and kidneys, leading to the life-threatening consequences seen in acute liver failure.[35] Therefore, the liver can be used as a therapeutic target to improve the prognosis of sepsis. Our study found that Roquin-1 might be used as a target in the treatment of SALI, while further research was needed to determine the function of Roquin-1 in sepsis-induced multiorgan dysfunction.

Few treatment approaches exist for septic organ injury. The management of intensive care patients relies on sufficient fluid restriction, stabilization of breathing, and infection treatment.[36] In the event of liver malfunction, organ replacement is difficult and laborious, and most bridges repair the liver within brief time intervals.[37] Multiple variables, including genetic predisposition, gender, current immunological condition, pre-existing damage, and the invading pathogen, influence the liver's response to infection.[38] This intricacy may be one reason why no particular therapeutic therapy for septic liver failure has been identified.[39] Moreover, preclinical studies suggest that individualized treatment for liver failure has the potential to enhance patient care and sepsis outcomes.[40] We determined that Roquin-1 in macrophage might relieve the SALI via miRNAs in MDEVs. We suppose that Roquin-1 and MDEVs can be applied as valuable targets in SALI treatment.

The liver is a prominent immune modulatory organ in which almost all immune and parenchymal cells perform diverse immunological roles.[41] The liver serves as the second line of defense after the intestinal barrier, transporting bacteria and their metabolites through the portal vein.[42] Under physiological settings, the accumulation of pro- and anti-inflammatory chemicals and pathways is essential for maintaining immunological homeostasis. In the case of systemic infection, alterations in inflammatory responses occur in a widespread immune response, which may lead to organ failure coordinated by parenchymal, non-parenchymal, and infiltrating immune cells in the liver.[43] Several studies have revealed the function of møs and Tregs during SALI. Both mouse and human liver-infiltrating møs display anti-inflammatory phenotypes and promote the wound-healing and tissue regeneration.[11] A previous study showed that programmed cell death-1 inhibited the bacterial clearance of møs and aggravated SALI.[44] Meanwhile, morbidity/mortality during sepsis is mediated by Tregs.[45] Our study found that the monocyte-derived mø was the primary source of Roquin-1and acted as a protector during SALI. Then, we revealed that Rouqin-1$^{san/san}$ in møs aggravated SALI by upregulating M1 frequency and decreasing the Treg ratio *in vivo* and *in vitro*.

In the studies of several disease models, the critical role of Roquin-1 as a post-transcriptional regulator of inflammatory responses is well described. Our study showed that Roquin-1 bond with AMPKa1 directly with its 133–1300 chain, regulated ubiquitination of the AMPKa1-K63 ubiquitin chain and modulated AMPKa1activity.[19] Previous research showed that nonsense Roquin-1 mutation upregulated $CD8^+$ T cells and Th17 cells *in vivo*.[46] Meanwhile, Roquin-1 interacted with Regnease-1 proteins on RNA, resulting in the spontaneous activation of T cells. Roquin-1 promoted $CD4^+$ T cells committed to the follicular helper T cell subset and enhanced the cytotoxic activity in $CD8^+$ T cells (14). However, most of the previous studies focused on the single cells instead of the systemic inflammatory response during SALI. Herein, we found that Roquin-1 in møs had a protective effect against SALI. Roquin-1$^{san/san}$ in møs reduced the Tregs differentiation and promoted M1 polarization via MEDVs. Meanwhile, the results showed that Roquin-1 in SALI patients and mice was decreased and correlated with the inflammatory profiles (M1 mø/Tregs/TNF-α/TGF-β/IL-6/IL-10). Therefore, to our knowledge, this is the first report to highlight the biological significance of Roquin-1in the protection of SALI.

Several studies have been conducted on the function of EVs in the past decade. All cells, prokaryotes, and eukaryotes release EVs as part of their normal physiology and during acquired abnormalities. EVs can be broadly divided into two categories, ectosomes and exosomes. Ectosomes are vesicles that pinch off the surface of the plasma membrane via outward budding and include multivesicular bodies, microparticles, and large vesicles in the size range of ~50 nm to 1 μm in diameter. Exosomes are EVs with a size range of ~40–160 nm (average ~100 nm) in diameter with an endosomal origin.[47] Because of the technical difficulties in isolating and purifying exosomes, especially in the sense of distinguishing them from other EVs, the International Society for Extracellular Vesicles (ISEV) encourages the use of "EVs" unless researchers can provide enough evidence for the identification of the vesicles they worked on within their experimental system.[48] Our study used TEM, NTA, and western blot to detect the EVs characters. The EVs that we isolated were 50–120nm CD63+Tsg101+ particles. Although the result showed that the EVs that we isolated were exosomes, we still used EVs to avoid confusion and misunderstanding.

EVs are novel immune therapies for multiple diseases involving inflammation or immune reaction. EVs have not only tissue repair-promoting properties but also immunosuppressive properties. M2 møs derived EVs represent a promising multifunctional nanotherapeutic for attenuating cytokine storms associated with infectious diseases.[49] Another study showed that EVs derived from M1 møs were engineered to induce M1 polarization to repress tumor growth.[50] Our study administered WT and Roquin-1$^{san/san}$ MDEVs in the SALI mouse model via tail vein injection and showed that WT MDEVs could ameliorate SALI in mice while

Roquin-1$^{san/san}$ could aggravate it. Our finding suggests that WT MDEVs may be an effective treatment for SALI. Further studies will be conducted to confirm the treatment of MDEVs in humans.

The question arises as to which mechanism may be involved in the function of MDEVs during SALI. It has been shown that EVs play both a pro-inflammatory and anti-inflammatory role during sepsis.[51] EVs have different effects depending on the sepsis stage and the type of derived cells. A recent study showed that mø uptake of necroptotic cell-derived EVs leads to the release of proinflammatory cytokines.[52] M2 møs transport TGF-β through MDEVs, promoting Tregs differentiation.[53] In our study, WT MDEVs promoted the differentiation of Tregs and inhibited M1 polarization via MDEVs *in vitro* and vivo, while Roquin-1$^{san/san}$ MDEVs performed the opposite function. Our study reveals a target to diagnose and treat SALI and determines a treatment protocol, MDEVs, that can be used to modulate mø and Treg synchronously.

Additionally, the mechanism that Roquin-1 modulates the function of MDEVs needs to be investigated. Among the substances transmitted by EVs, miRNAs are the most widely studied. According to high-throughput sequencing, the selected miRNAs were not identical in møs and MDEVs. Notably, compared with the WT group, some miRNAs in Roquin-1$^{san/san}$ MDEVs changed significantly, while the homologous miRNAs in Roquin-1$^{san/san}$ møs did not change significantly. Conversely, the other miRNAs, which changed dramatically in møs, did not change in MDEVs. The RNAs in EVs are combined with RNA-binding proteins and lipoproteins.[54] RNA-induced silencing complex, including Ago2 and RNAs, control RNA sorting in EVs.[55,56] Here, our study has shown that Roquin-1modulated miRNA sorting in MDEVs by promoting the location of Ago2 in MVE and the binding between Ago2 and selected RNA. Previous studies have indicated that the N-terminal domain of Ago2 regulated the binding between Ago2 and miRNAs to medicate the miRNAs metabolism.[57] In this study, by analyzing the motifs of møs-miRNAs and MDEVs-miRNAs, we observed that Roquin-1 sorted selected miRNAs into MDEVs by miRNAs motifs. Furthermore, it has previously been observed that the phosphorylation at the serine/threonine site played a critical role in Ago2-miRNA interactions.[57] In this study, our mass spectrum analysis of Ago2 showed that the phosphorylation sites included S387 and S828. Moreover, we examined the role of Ago2-S387 and Ago2-S828, respectively. Unlike Ago2-S387 phosphorylation, which inhibited Ago2 location in MVE and secretion in MDEVs, Ago2-S828 significantly changed the connection between Ago2 and selected miRNAs. Summarily, Roquin-1 binds with Ago2 by the RING domain to promote the Ago2-K258 ubiquitination and suppress the Ago2-S387/828 phosphorylation.

Finally, by selectively deleting three putative micro-RNAs reported to be abundant in MDEVs, a source for the anti-inflammatory signaling by MDEVs was identified. The absence of miR-let-7a, miR-486a, or miR-146a in MDEVs dramatically reduced their ability to inhibit M1 polarization and promote Tregs differentiation. These results indicate that the intercellular communication of these three microRNAs through MDEVs is crucial to our observations. It has been demonstrated that miR-let-7a in MDEVs controls the PI3K-Akt signaling pathway to promote M2 polarization.[58] Additionally, it has been found that miR-486a inhibited the transcriptional activity of NLRP3.[59] Similarly, EVs produced from the liver of mice infected with Schistosoma japonicum deliver miR-142a-3p to target WASL and inhibit CCL2 expression.[60] In our study, the expressions of these three miRNAs in plasma EV of SALI patients were significantly lower than these in health person. Meanwhile, our *in vitro* results showed that these three miRNAs upregulate Tregs differentiation and inhibit the polarization of M1 mø. These observations support the notion that each of these three microRNAs carried by MDEVs contributes to the regulation of inflammatory responses by targeting distinct gene sets that affect TSC22D2-STAT3 signaling in T cells and TSC22D2-AMPKα-mTOR in mø. Furthermore, according to previous studies, STAT3 is a double-edged sword that activates immune cell immunity and immunosuppression. STAT3 inhibition reduced TGF-β of the gastric bulb and decreased Treg by increasing Th17 cells and IFNγ.[61] On the other hand, miR-let-7f in bone marrow-derived mesenchymal stem cells inhibited STAT3 activity decreased Th17 cell levels and upregulated the Tregs ratio.[62] Our results accord with previous studies indicating that the miRNAs in WT MDEVs inhibit STAT3-phosphorylation and promote Tregs differentiation. At the same time, MDEVs did not affect the suppressive function of Tregs. Meanwhile, Renal carcinoma-derived EVs tRNA by increasing STAT3 activation and promoting the M1 polarization.[63] Our research analyzed the role of MDEVs in STAT3 activation in BMDM. However, our results suggest that WT/Roquin-1$^{san/san}$ MDEVs could not affect the phosphorylation of STAT3. A previous study showed that Annexin A1 inhibited AMPKα, upregulated the downstream target of mTOR and decreased the M1 polarization.[27] Consistent with previous studies, we revealed that miRNAs in WT MDEVs reduced the AMPKα-phosphorylation and upregulated the mTOR-phosphorylation, while miRNAs in Roquin-1$^{san/san}$ MDEVs showed the opposite effect. Finally, TSC22D2 is a member of the leucine zipper transcription factor transforming growth factor-stimulated clone 22 (TSC-22) domain family. There are currently

few publications on the function of TSC22D2, and research on the role and mechanism of TSC22D2 in the etiology and pathophysiology of immune-related disease is limited.[64] Our work discovered that TSC22D2 is related to STAT3 signaling in Tregs and AMPKα/mTOR pathway in mø. Consequently, we hypothesize that TSC22D2 may play a vital role in the occurrence and development of immune-related disease, which in conjunction with many immune cells differentiation/polarization, might lead to a change in the regulatory network, ultimately resulting in the development of immune response during sepsis.

In summary, we identify a previously unrecognized role of Roqiun-1 in SALI. Roquin-1 alleviates SALI by promoting MDEVs-miRNAs (miR-let-7a/miR-486a/miR-142a), mediating differentiation of Tregs via TSC22D2-STAT3 signaling, and inhibiting M1 polarization by the TSC22D2-AMPKα/mTOR pathway synchronous. Furthermore, Roquin-1 announced Ago2 and miRNAs sorting in MDEVs by upregulating the ubiquitination of Ago2-K258 and inhibiting its phosphorylation at S387 and S828. Our study provides a novel perspective for revealing the mechanism of SALI and offers targets for clinical intervention in SALI.

Limitations of the study

This study has some limitations. At first, EVs are transporters of mRNA, miRNA, cytokines, proteins, enzymes, molecular chaperones, and signal molecules. We investigated the function and mechanism of miRNA between WT and Roquin-1$^{san/san}$ MDEVs. The change in mRNA, cytokines and proteins still needs to be researched. Meanwhile, we observed that Roquin-1$^{san/san}$ increased the bind between Ago2 and miR-18a and the location of the Ago2-miR-18a complex in the P-body. At the same time, the miR-18a in Roquin-1$^{san/san}$ BMDM decreased. Previous studies revealed that P-body could regulate miRNA decay and its binding to target mRNAs.[65] We speculated that miR-18a might be decomposed in P-body. However, the detailed mechanism that Roquin-1 induces the decrease of miR-18a in BMDM remains further investigated. Finally, sepsis usually induces the systemic syndrome including multiorgan dysfunction. Although the liver plays a critical role during sepsis, every organ has its own characteristic features in immune response during sepsis. We need to investigate the function of Roquin-1 and MDEVs in other organs in the future.

STAR★METHODS

Detailed methods are provided in the online version of this paper and include the following:

- KEY RESOURCES TABLE
- RESOURCE AVAILABILITY
  - Lead contact
  - Materials availability
  - Data and code availability
- EXPERIMENTAL MODEL AND STUDY PARTICIPANT DETAILS
  - Clinical data and samples collection
  - Mice in this study
  - Cells and reagents
  - Chimeric mice
  - Sepsis-induced liver failure model in mice
  - Macrophage isolation in mice liver
  - Bone marrow-derived macrophage culture
  - Isolation of naïve T cells and induction of Tregs-differentiation
  - Primary hepatocyte sorting and culture in mice
- METHOD DETAILS
  - Macrophage-derived extracellular vesicles isolation
  - Coculture of møs/MDEVs and Tregs
  - The absorption of MDEVs
  - Subcellular fractionation
  - Plasmid construction
  - Point mutation plasmid construction
  - Lentiviral infection
  - Transfection of siRNA
  - Suppressive activity of Tregs *in vitro*
  - Immunoprecipitation
  - The use of MDEVs, STAT3 and AMPKα activators/inhibitors

- Histology and immunofluorescence stains in tissue
- Immunofluorescence stain in cells
- Transmission electron microscopy
- RNA Binding Protein Immunoprecipitation (RIP)
- Flow cytometry
- Western blot analysis
- MiRNA sequence assays
- Qualitative RT-PCR analysis
- ELISA
- miRNA pulldown
- Luciferase assay
- Study approval
- Statistical analysis

- QUANTIFICATION AND STATISTICAL ANALYSIS

SUPPLEMENTAL INFORMATION

Supplemental information can be found online at https://doi.org/10.1016/j.isci.2023.107295.

ACKNOWLEDGMENTS

This work was supported by grants from the National Nature Science Foundation of China (82071798 , 81600450 and 81871260), Six Talent Peaks Project in Jiangsu Province (No. 2018-WSN-011), Jiangsu Science and Technology Association Young Science and Technology Talents Lifting Project (No. DG000D4007), National Science Foundation of Jiangsu Province (BK20191490), Clinical Research Program in Shanghai 9th people's hospital(JYLJ022), Research Project of Health and Family Planning Commission in Pudong New Area (PW2018D-01), Seed Foundation in Shanghai Ninth People's Hospital (JYZZ091), A project funded by the PAPD and China Scholarship Council.

AUTHOR CONTRIBUTIONS

L.Z. researched data and contributed to discussion. D.Z. and Z.L. assisted animal feeding and experiments and provided other technical assistance. Z.L. and W.L. wrote the manuscript. L.K. and Y.L. contributed to discussion and reviewed/edited manuscript. L.Z. and H.Z. designed the study, and revised/edited manuscript.

DECLARATION OF INTERESTS

The authors have declared that no conflict of interest exists.

INCLUSION AND DIVERSITY

We support inclusive, diverse, and equitable conduct of research.

Received: May 29, 2022
Revised: January 5, 2023
Accepted: July 3, 2023
Published: July 12, 2023

REFERENCES

1. van der Poll, T., Shankar-Hari, M., and Wiersinga, W.J. (2021). The immunology of sepsis. Immunity *54*, 2450–2464. https://doi.org/10.1016/j.immuni.2021.10.012.

2. Sygitowicz, G., and Sitkiewicz, D. (2020). Molecular mechanisms of organ damage in sepsis: an overview. Braz. J. Infect. Dis. *24*, 552–560. https://doi.org/10.1016/j.bjid.2020.09.004.

3. Jacobi, J. (2022). The pathophysiology of sepsis - 2021 update: Part 2, organ dysfunction and assessment. Am. J. Health Syst. Pharm. *79*, 424–436. https://doi.org/10.1093/ajhp/zxab393.

4. Kübler, A., Adamik, B., Durek, G., Mayzner-Zawadzka, E., Gaszyński, W., Karpel, E., and Duszyńska, W. (2015). Results of the severe sepsis registry in intensive care units in Poland from 2003-2009. Anaesthesiol. Intensive Ther. *47*, 7–13. https://doi.org/10.5603/AIT.2015.0002.

5. Woźnica, E.A., Inglot, M., Woźnica, R.K., and Łysenko, L. (2018). Liver dysfunction in sepsis. Adv. Clin. Exp. Med. *27*, 547–551. https://doi.org/10.17219/acem/68363.

6. Tujios, S., Stravitz, R.T., and Lee, W.M. (2022). Management of Acute Liver Failure: Update 2022. Semin. Liver Dis. *42*, 362–378. https://doi.org/10.1055/s-0042-1755274.

7. Gazdic, M., Markovic, B.S., Arsenijevic, A., Jovicic, N., Acovic, A., Harrell, C.R., Fellabaum, C., Djonov, V., Arsenijevic, N., Lukic, M.L., and Volarevic, V. (2018). Crosstalk between mesenchymal stem cells and T regulatory cells is crucially important for the

attenuation of acute liver injury. Liver Transplant. *24*, 687–702. https://doi.org/10.1002/lt.25049.

8. Biagioli, M., Carino, A., Fiorucci, C., Marchianò, S., Di Giorgio, C., Bordoni, M., Roselli, R., Baldoni, M., Distrutti, E., Zampella, A., and Fiorucci, S. (2020). The Bile Acid Receptor GPBAR1 Modulates CCL2/CCR2 Signaling at the Liver Sinusoidal/Macrophage Interface and Reverses Acetaminophen-Induced Liver Toxicity. J. Immunol. *204*, 2535–2551. https://doi.org/10.4049/jimmunol.1901427.

9. Krenkel, O., and Tacke, F. (2017). Liver macrophages in tissue homeostasis and disease. Nat. Rev. Immunol. *17*, 306–321. https://doi.org/10.1038/nri.2017.11.

10. Nakagaki, B.N., Mafra, K., de Carvalho, É., Lopes, M.E., Carvalho-Gontijo, R., de Castro-Oliveira, H.M., Campolina-Silva, G.H., de Miranda, C.D.M., Antunes, M.M., Silva, A.C.C., et al. (2018). Immune and metabolic shifts during neonatal development reprogram liver identity and function. J. Hepatol. *69*, 1294–1307. https://doi.org/10.1016/j.jhep.2018.08.018.

11. Triantafyllou, E., Woollard, K.J., McPhail, M.J.W., Antoniades, C.G., and Possamai, L.A. (2018). The Role of Monocytes and Macrophages in Acute and Acute-on-Chronic Liver Failure. Front. Immunol. *9*, 2948. https://doi.org/10.3389/fimmu.2018.02948.

12. Zheng, L., Li, Z., Ling, W., Zhu, D., Feng, Z., and Kong, L. (2018). Exosomes Derived from Dendritic Cells Attenuate Liver Injury by Modulating the Balance of Treg and Th17 Cells After Ischemia Reperfusion. Cell. Physiol. Biochem. *46*, 740–756. https://doi.org/10.1159/000488733.

13. Strnad, P., Tacke, F., Koch, A., and Trautwein, C. (2017). Liver - guardian, modifier and target of sepsis. Nat. Rev. Gastroenterol. Hepatol. *14*, 55–66. https://doi.org/10.1038/nrgastro.2016.168.

14. Schaefer, J.S., and Klein, J.R. (2016). Roquin–a multifunctional regulator of immune homeostasis. Gene Immun. *17*, 79–84. https://doi.org/10.1038/gene.2015.58.

15. Srivastava, M., Duan, G., Kershaw, N.J., Athanasopoulos, V., Yeo, J.H.C., Ose, T., Hu, D., Brown, S.H.J., Jergic, S., Patel, H.R., et al. (2015). Roquin binds microRNA-146a and Argonaute2 to regulate microRNA homeostasis. Nat. Commun. *6*, 6253. https://doi.org/10.1038/ncomms7253.

16. Lee, S.Y., Moon, S.J., Kim, E.K., Seo, H.B., Yang, E.J., Son, H.J., Kim, J.K., Min, J.K., Park, S.H., and Cho, M.L. (2017). Metformin Suppresses Systemic Autoimmunity in Roquin(san/san) Mice through Inhibiting B Cell Differentiation into Plasma Cells via Regulation of AMPK/mTOR/STAT3. J. Immunol. *198*, 2661–2670. https://doi.org/10.4049/jimmunol.1403088.

17. Ramiscal, R.R., Parish, I.A., Lee-Young, R.S., Babon, J.J., Blagih, J., Pratama, A., Martin, J., Hawley, N., Cappello, J.Y., Nieto, P.F., et al. (2015). Attenuation of AMPK signaling by ROQUIN promotes T follicular helper cell formation. Elife *4*, e08698. https://doi.org/10.7554/eLife.08698.

18. Bari, S.M.I., Hossain, F.B., and Nestorova, G.G. (2021). Advances in Biosensors Technology for Detection and Characterization of Extracellular Vesicles. Sensors *21*, 7645. https://doi.org/10.3390/s21227645.

19. Zheng, L., Ling, W., Zhu, D., Li, Z., and Kong, L. (2020). Roquin-1 Regulates Macrophage Immune Response and Participates in Hepatic Ischemia-Reperfusion Injury. J. Immunol. *204*, 1322–1333. https://doi.org/10.4049/jimmunol.1900053.

20. Murao, A., Brenner, M., Aziz, M., and Wang, P. (2020). Exosomes in Sepsis. Front. Immunol. *11*, 2140. https://doi.org/10.3389/fimmu.2020.02140.

21. Wang, G., Jin, S., Ling, X., Li, Y., Hu, Y., Zhang, Y., Huang, Y., Chen, T., Lin, J., Ning, Z., et al. (2019). Proteomic Profiling of LPS-Induced Macrophage-Derived Exosomes Indicates Their Involvement in Acute Liver Injury. Proteomics *19*, e1800274. https://doi.org/10.1002/pmic.201800274.

22. Njock, M.S., Cheng, H.S., Dang, L.T., Nazari-Jahantigh, M., Lau, A.C., Boudreau, E., Roufaiel, M., Cybulsky, M.I., Schober, A., and Fish, J.E. (2015). Endothelial cells suppress monocyte activation through secretion of extracellular vesicles containing antiinflammatory microRNAs. Blood *125*, 3202–3212. https://doi.org/10.1182/blood-2014-11-611046.

23. Bouchareychas, L., Duong, P., Covarrubias, S., Alsop, E., Phu, T.A., Chung, A., Gomes, M., Wong, D., Meechoovet, B., Capili, A., et al. (2020). Macrophage Exosomes Resolve Atherosclerosis by Regulating Hematopoiesis and Inflammation via MicroRNA Cargo. Cell Rep. *32*, 107881. https://doi.org/10.1016/j.celrep.2020.107881.

24. Fabbiano, F., Corsi, J., Gurrieri, E., Trevisan, C., Notarangelo, M., and D'Agostino, V.G. (2020). RNA packaging into extracellular vesicles: An orchestra of RNA-binding proteins? J. Extracell. Vesicles *10*, e12043. https://doi.org/10.1002/jev2.12043.

25. Zhang, Y., Liu, Y., Liu, H., and Tang, W.H. (2019). Exosomes: biogenesis, biologic function and clinical potential. Cell Biosci. *9*, 19. https://doi.org/10.1186/s13578-019-0282-2.

26. Yu, H., Qin, L., Peng, Y., Bai, W., and Wang, Z. (2020). Exosomes Derived From Hypertrophic Cardiomyocytes Induce Inflammation in Macrophages via miR-155 Mediated MAPK Pathway. Front. Immunol. *11*, 606045. https://doi.org/10.3389/fimmu.2020.606045.

27. Xu, X., Gao, W., Li, L., Hao, J., Yang, B., Wang, T., Li, L., Bai, X., Li, F., Ren, H., et al. (2021). Annexin A1 protects against cerebral ischemia-reperfusion injury by modulating microglia/macrophage polarization via FPR2/ALX-dependent AMPK-mTOR pathway. J. Neuroinflammation *18*, 119. https://doi.org/10.1186/s12974-021-02174-3.

28. Grondman, I., Pirvu, A., Riza, A., Ioana, M., and Netea, M.G. (2020). Biomarkers of inflammation and the etiology of sepsis. Biochem. Soc. Trans. *48*, 1–14. https://doi.org/10.1042/BST20190029.

29. Sakr, Y., Jaschinski, U., Wittebole, X., Szakmany, T., Lipman, J., Namendys-Silva, S.A., Martin-Loeches, I., Leone, M., Lupu, M.N., and Vincent, J.L.; ICON Investigators (2018). Sepsis in Intensive Care Unit Patients: Worldwide Data From the Intensive Care over Nations Audit. Open Forum Infect. Dis. *5*, ofy313. https://doi.org/10.1093/ofid/ofy313.

30. Jin, L., Zhao, C., Li, H., Wang, R., Wang, Q., and Wang, H. (2021). Clinical Profile, Prognostic Factors, and Outcome Prediction in Hospitalized Patients With Bloodstream Infection: Results From a 10-Year Prospective Multicenter Study. Front. Med. *8*, 629671. https://doi.org/10.3389/fmed.2021.629671.

31. Zhang, J., Zhao, C., Chen, H., Li, H., Wang, Q., Wang, Z., Zhang, F., and Wang, H.; CARES Network (2018). A multicenter epidemiology study on the risk factors and clinical outcomes of nosocomial intra-abdominal infections in China: results from the Chinese Antimicrobial Resistance Surveillance of Nosocomial Infections (CARES) 2007-2016. Infect. Drug Resist. *11*, 2311–2319. https://doi.org/10.2147/IDR.S182180.

32. Bauer, M., Coldewey, S.M., Leitner, M., Löffler, B., Weis, S., and Wetzker, R. (2018). Deterioration of Organ Function As a Hallmark in Sepsis: The Cellular Perspective. Front. Immunol. *9*, 1460. https://doi.org/10.3389/fimmu.2018.01460.

33. Sun, J., Zhang, J., Wang, X., Ji, F., Ronco, C., Tian, J., and Yin, Y. (2020). Gut-liver crosstalk in sepsis-induced liver injury. Crit. Care *24*, 614. https://doi.org/10.1186/s13054-020-03327-1.

34. Kasper, P., Tacke, F., Steffen, H.M., and Michels, G. (2020). [Hepatic dysfunction in sepsis]. Med. Klin. Intensivmed. Notfallmed. *115*, 609–619. https://doi.org/10.1007/s00063-020-00707-x.

35. Sabapathy, D.G., and Desai, M.S. (2022). Acute Liver Failure in Children. Pediatr. Clin. *69*, 465–495. https://doi.org/10.1016/j.pcl.2022.02.003.

36. Dugar, S., Choudhary, C., and Duggal, A. (2020). Sepsis and septic shock: Guideline-based management. Cleve. Clin. J. Med. *87*, 53–64. https://doi.org/10.3949/ccjm.87a.18143.

37. Nguyen, A., Mirza, S., Javed, N., Hanif, H., Ryu, M., Mirza, R.T., and Sheikh, A.B. (2022). Extracorporeal Liver Support: An Updated Review of Mechanisms and Current Literature. J. Community Hosp. Intern. Med. Perspect. *12*, 43–48. https://doi.org/10.55729/2000-9666.1064.

38. Schaarschmidt, B., Vlaic, S., Medyukhina, A., Neugebauer, S., Nietzsche, S., Gonnert, F.A., Rödel, J., Singer, M., Kiehntopf, M., Figge, M.T., et al. (2018). Molecular signatures of liver dysfunction are distinct in fungal and bacterial infections in mice. Theranostics *8*, 3766–3780. https://doi.org/10.7150/thno.24333.

39. Canabal, J.M., and Kramer, D.J. (2008). Management of sepsis in patients with liver failure. Curr. Opin. Crit. Care *14*, 189–197. https://doi.org/10.1097/MCC.0b013e3282f6a435.

40. Itenov, T.S., Murray, D.D., and Jensen, J.U.S. (2018). Sepsis: Personalized Medicine Utilizing 'Omic' Technologies-A Paradigm Shift? Healthcare *6*, 111. https://doi.org/10.3390/healthcare6030111.

41. Cheng, M.L., Nakib, D., Perciani, C.T., and MacParland, S.A. (2021). The immune niche of the liver. Clin. Sci. *135*, 2445–2466. https://doi.org/10.1042/CS20190654.

42. Beyer, D., Hoff, J., Sommerfeld, O., Zipprich, A., Gaßler, N., and Press, A.T. (2022). The liver in sepsis: molecular mechanism of liver failure and their potential for clinical translation. Mol. Med. *28*, 84. https://doi.org/10.1186/s10020-022-00510-8.

43. Carranza-Trejo, A.M., Vetvicka, V., Vistejnova, L., Kralickova, M., and Montufar, E.B. (2021). Hepatocyte and immune cell crosstalk in non-alcoholic fatty liver disease. Expet Rev. Gastroenterol. Hepatol. *15*, 783–796. https://doi.org/10.1080/17474124.2021.1887730.

44. Triantafyllou, E., Gudd, C.L., Mawhin, M.A., Husbyn, H.C., Trovato, F.M., Siggins, M.K., O'Connor, T., Kudo, H., Mukherjee, S.K., Wendon, J.A., et al. (2021). PD-1 blockade improves Kupffer cell bacterial clearance in acute liver injury. J. Clin. Invest. *131*, e140196. https://doi.org/10.1172/JCI140196.

45. Gray, C.C., Biron-Girard, B., Wakeley, M.E., Chung, C.S., Chen, Y., Quiles-Ramirez, Y., Tolbert, J.D., and Ayala, A. (2022). Negative Immune Checkpoint Protein, VISTA, Regulates the CD4(+) Treg Population During Sepsis Progression to Promote Acute Sepsis Recovery and Survival. Front. Immunol. *13*, 861670. https://doi.org/10.3389/fimmu.2022.861670.

46. Tavernier, S.J., Athanasopoulos, V., Verloo, P., Behrens, G., Staal, J., Bogaert, D.J., Naesens, L., De Bruyne, M., Van Gassen, S., Parthoens, E., et al. (2019). A human immune dysregulation syndrome characterized by severe hyperinflammation with a homozygous nonsense Roquin-1 mutation. Nat. Commun. *10*, 4779. https://doi.org/10.1038/s41467-019-12704-6.

47. Kalluri, R., and LeBleu, V.S. (2020). The biology, function, and biomedical applications of exosomes. Science *367*, eaau6977. https://doi.org/10.1126/science.aau6977.

48. Théry, C., Witwer, K.W., Aikawa, E., Alcaraz, M.J., Anderson, J.D., Andriantsitohaina, R., Antoniou, A., Arab, T., Archer, F., Atkin-Smith, G.K., et al. (2018). Minimal information for studies of extracellular vesicles 2018 (MISEV2018): a position statement of the International Society for Extracellular Vesicles and update of the MISEV2014 guidelines. J. Extracell. Vesicles *7*, 1535750. https://doi.org/10.1080/20013078.2018.1535750.

49. Wang, Y., Liu, S., Li, L., Li, L., Zhou, X., Wan, M., Lou, P., Zhao, M., Lv, K., Yuan, Y., et al. (2022). Peritoneal M2 macrophage-derived extracellular vesicles as natural multitarget nanotherapeutics to attenuate cytokine storms after severe infections. J. Contr. Release *349*, 118–132. https://doi.org/10.1016/j.jconrel.2022.06.063.

50. Gunassekaran, G.R., Poongkavithai Vadevoo, S.M., Baek, M.C., and Lee, B. (2021). M1 macrophage exosomes engineered to foster M1 polarization and target the IL-4 receptor inhibit tumor growth by reprogramming tumor-associated macrophages into M1-like macrophages. Biomaterials *278*, 121137. https://doi.org/10.1016/j.biomaterials.2021.121137.

51. Burgelman, M., Vandendriessche, C., and Vandenbroucke, R.E. (2021). Extracellular Vesicles: A Double-Edged Sword in Sepsis. Pharmaceuticals *14*, 829. https://doi.org/10.3390/ph14080829.

52. Shlomovitz, I., Erlich, Z., Arad, G., Edry-Botzer, L., Zargarian, S., Cohen, H., Manko, T., Ofir-Birin, Y., Cooks, T., Regev-Rudzki, N., and Gerlic, M. (2021). Proteomic analysis of necroptotic extracellular vesicles. Cell Death Dis. *12*, 1059. https://doi.org/10.1038/s41419-021-04317-z.

53. Vogel, K.U., Edelmann, S.L., Jeltsch, K.M., Bertossi, A., Heger, K., Heinz, G.A., Zöller, J., Warth, S.C., Hoefig, K.P., Lohs, C., et al. (2013). Roquin paralogs 1 and 2 redundantly repress the Icos and Ox40 costimulator mRNAs and control follicular helper T cell differentiation. Immunity *38*, 655–668. https://doi.org/10.1016/j.immuni.2012.12.004.

54. Iraci, N., Leonardi, T., Gessler, F., Vega, B., and Pluchino, S. (2016). Focus on Extracellular Vesicles: Physiological Role and Signalling Properties of Extracellular Membrane Vesicles. Int. J. Mol. Sci. *17*, 171. https://doi.org/10.3390/ijms17020171.

55. Villarroya-Beltri, C., Baixauli, F., Gutiérrez-Vázquez, C., Sánchez-Madrid, F., and Mittelbrunn, M. (2014). Sorting it out: regulation of exosome loading. Semin. Cancer Biol. *28*, 3–13. https://doi.org/10.1016/j.semcancer.2014.04.009.

56. Treiber, T., Treiber, N., and Meister, G. (2019). Regulation of microRNA biogenesis and its crosstalk with other cellular pathways. Nat. Rev. Mol. Cell Biol. *20*, 5–20. https://doi.org/10.1038/s41580-018-0059-1.

57. Quévillon Huberdeau, M., Zeitler, D.M., Hauptmann, J., Bruckmann, A., Fressigné, L., Danner, J., Piquet, S., Strieder, N., Engelmann, J.C., Jannot, G., et al. (2017). Phosphorylation of Argonaute proteins affects mRNA binding and is essential for microRNA-guided gene silencing *in vivo*. EMBO J. *36*, 2088–2106. https://doi.org/10.15252/embj.201696386.

58. Li, K., Yan, G., Huang, H., Zheng, M., Ma, K., Cui, X., Lu, D., Zheng, L., Zhu, B., Cheng, J., and Zhao, J. (2022). Anti-inflammatory and immunomodulatory effects of the extracellular vesicles derived from human umbilical cord mesenchymal stem cells on osteoarthritis via M2 macrophages. J. Nanobiotechnol. *20*, 38. https://doi.org/10.1186/s12951-021-01236-1.

59. Zhang, C., Gong, Y., Li, N., Liu, X., Zhang, Y., Ye, F., Guo, Q., and Zheng, J. (2021). Long noncoding RNA Kcnq1ot1 promotes sC5b-9-induced podocyte pyroptosis by inhibiting miR-486a-3p and upregulating NLRP3. Am. J. Physiol. Cell Physiol. *320*, C355–C364. https://doi.org/10.1152/ajpcell.00403.2020.

60. Wang, L., Zhu, Z., Liao, Y., Zhang, L., Yu, Z., Yang, R., Wu, J., Wu, Z., and Sun, X. (2022). Host liver-derived extracellular vesicles deliver miR-142a-3p induces neutrophil extracellular traps via targeting WASL to block the development of Schistosoma japonicum. Mol. Ther. *30*, 2092–2107. https://doi.org/10.1016/j.ymthe.2022.03.016.

61. Hajimoradi, M., Rezalotfi, A., Esmaeilnejad-Ahranjani, P., Mohammad Hassan, Z., and Ebrahimi, M. (2022). STAT3 inactivation suppresses stemness properties in gastric cancer stem cells and promotes Th17 in Treg/Th17 balance. Int. Immunopharm. *111*, 109048. https://doi.org/10.1016/j.intimp.2022.109048.

62. Geng, L., Tang, X., Wang, S., Sun, Y., Wang, D., Tsao, B.P., Feng, X., and Sun, L. (2020). Reduced Let-7f in Bone Marrow-Derived Mesenchymal Stem Cells Triggers Treg/Th17 Imbalance in Patients With Systemic Lupus Erythematosus. Front. Immunol. *11*, 233. https://doi.org/10.3389/fimmu.2020.00233.

63. Zhang, W., Zheng, X., Yu, Y., Zheng, L., Lan, J., Wu, Y., Liu, H., Zhao, A., Huang, H., and Chen, W. (2022). Renal cell carcinoma-derived exosomes deliver lncARSR to induce macrophage polarization and promote tumor progression via STAT3 pathway. Int. J. Biol. Sci. *18*, 3209–3222. https://doi.org/10.7150/ijbs.70289.

64. Xiao, L., Wei, F., Liang, F., Li, Q., Deng, H., Tan, S., Chen, S., Xiong, F., Guo, C., Liao, Q., et al. (2019). TSC22D2 identified as a candidate susceptibility gene of multi-cancer pedigree using genome-wide linkage analysis and whole-exome sequencing. Carcinogenesis *40*, 819–827. https://doi.org/10.1093/carcin/bgz095.

65. Brothers, W.R., Fakim, H., Kajjo, S., and Fabian, M.R. (2022). P-bodies directly regulate MARF1-mediated mRNA decay in human cells. Nucleic Acids Res. *50*, 7623–7636. https://doi.org/10.1093/nar/gkac557.

66. Love, M.I., Huber, W., and Anders, S. (2014). Moderated estimation of fold change and dispersion for RNA-seq data with DESeq2. Genome Biol. *15*, 550. https://doi.org/10.1186/s13059-014-0550-8.

67. Wagih, O. (2017). ggseqlogo: a versatile R package for drawing sequence logos. Bioinformatics *33*, 3645–3647. https://doi.org/10.1093/bioinformatics/btx469.

STAR★METHODS

KEY RESOURCES TABLE

REAGENT or RESOURCE	SOURCE	IDENTIFIER
Antibodies		
Roquin-1	Invitrogen	PA5-34519
CD11b	Novus	NB110-89474
F4/80	Novus	NB600-404
CX3CR1	Novus	NBP1-76949
Clec4F	Novus	AF2784
TSC22D2	Novus	NBP2-46238
Ago2	Abcam	186733
p-Ago2	Abcam	215746
Dcp1a	Abcam	240275
CD63	Abcam	217345
Tsg101	Abcam	125011
Flot1	Abcam	133497
Rab7	Abcam	137029
GW182	Abcam	70522
HSP70	Abcam	2787
Dicer	Abcam	14601
STAT3	Abcam	68153
p-STAT3	Abcam	267373
Flag	Abcam	205606
AMPKα	Abcam	32047
p-AMPKα	Abcam	210714
mTOR	Abcam	134903
p-mTOR	Abcam	109268
anti-CD11c PerCP-Cy5.5	Biolegend	117327
anti-CD11b PE-Cy7	Biolegend	101215
anti-CD206 APC	Biolegend	141707
anti-CD4 FITC	Biolegend	100405
anti-CD25 APC-Cy5.5	Biolegend	162105
anti-CD45-FITC	Biolegend	304006
anti-CD11b-APC	Biolegend	301410
anti-CD14-APC-Cy7	Biolegend	367108
anti-CCR2-BV605	Biolegend	357214
anti-mouse IgG PE	Biolegend	405307
anti-F4/80-APC-Cy7	Biolegend	157304
anti-FoxP3 PE	Biolegend	126403
Experimental models: Cell lines		
L929 Cell	ATCC	CCL-1
Mouse primary Bone marrow deriver macrophage	NA	NA
Mouse primary naïve T cell	NA	NA
Mouse primary hepatocyte	NA	NA

(*Continued on next page*)

Continued

REAGENT or RESOURCE	SOURCE	IDENTIFIER
Chemicals, peptides, and recombinant proteins		
GW4869	Selleckchem	S7609
LPS	Sigma	L4516
TGF-β1	Biolegend	763102
IL-2	Biolegend	575409
STAT3 inhibitor	MCE	HY-151976
AMPKα activator/inhibitor	MCE	HY-13417
AMPKα inhibitor	MCE	HY-151361
Lipo2000	Thermo Fisher	11668027
Critical commercial assays		
$CD4^+$ naïve T cell Isolation Kit	Miltenyi Biotec	130-104-453
Macrophage Isolation Kit and naïve T cell Isolation Kit	Miltenyi Biotec	130-110-434
Regents in qRT-PCR	Vazyme	MQ101-01/02
ALT ELISA kits	Abcam	Ab282882
AST ELISA kits	Abcam	ab138878
IL-10 ELISA Kits	LiankeBio	EK210
IL-6 ELISA Kits	LiankeBio	EK206
TNF-α ELISA Kits	Lianke Bio	EK282
TGF-β ELISA Kits	Lianke Bio	EK981
Deposited data		
miRNA sequeuce in macrophage and vesicles	This paper	GSE169215
Experimental models: Organisms/strains		
Roquin-1 san/san mouse	lead contact	NA
Experimental models: Cell lines		
L929 Cell	ATCC	CCL-1
Oligonucleotides		
pLenti-FLAG-Ago2	Hanheng Bio	NA
pLenti-FLAG-Roquin-1	Hanheng Bio	NA
pLenti-FLAG-Roquin-1133-1130	Hanheng Bio	NA
Si-Roquin-1	Hanheng Bio	NA
Si-Ago2-1	Hanheng Bio	NA
Si-Ago2-1	Hanheng Bio	NA
Si-STAT3	Hanheng Bio	NA
Si-Ago2-1	Hanheng Bio	NA
Si-Ago2-2	Hanheng Bio	NA
Si-STAT3	Hanheng Bio	NA
miR-let-7a inhibitor	GenePharma	NA
miR-142a inhibitor	GenePharma	NA
TSC22D2 inhibitor	GenePharma	NA
Non-specific inhibitor (NSI)	GenePharma	NA
miR-486a inhibitor	GenePharma	NA
Roquin-1	GenePharma	NA
IFN-γ	GenePharma	NA

(*Continued on next page*)

Continued

REAGENT or RESOURCE	SOURCE	IDENTIFIER
TNF-α	GenePharma	NA
TGF-β	GenePharma	NA
Foxp3	GenePharma	NA
IL-1α	GenePharma	NA
IL-2	GenePharma	NA
IL-13	GenePharma	NA
STAT3	GenePharma	NA
β-actin	GenePharma	NA
Let-7a	GenePharma	NA
miR-18a	GenePharma	NA
miR-486a	GenePharma	NA
miR-142a	GenePharma	NA
U6	GenePharma	NA
Software and algorithms		
ImageJ	Rawak Software	
SPSS	IBM	
FlowJo	FlowJo	Version 10
Graphprism	GraphPad	Version 8
R language	R Core Team	4.0.3
Dseq2	Love et al.[66]	https://bioconductor.org/packages/release/bioc/html/DESeq2.html
Ggseqlogo	Wagih[67]	https://cran.r-project.org/web/packages/ggseqlogo

RESOURCE AVAILABILITY

Lead contact

Further information and requests for resources and reagents should be directed to and will be fulfilled by the lead contact, Lianbao Kong (lbkong@njmu.edu.cn).

Materials availability

This study did not generate new unique reagents.

Data and code availability

- The miRNA sequence data was uploaded to the databank (GSE169215). Upon request, the lead contact will share all the data presented in this paper.
- All original code has been uploaded to GitHub and is accessible to the public via the following link as of the publication date: https://github.com/blanchzl/miRNA-sequence-in-roquin-1.
- Upon request, Lianbao Kong (lbkong@njmu.edu.cn) will provide any additional information necessary to reanalyze the data presented in this article.

EXPERIMENTAL MODEL AND STUDY PARTICIPANT DETAILS

Clinical data and samples collection

Our study was performed in patients with SALI, defined by the sepsis-induced occurrence of encephalopathy and hepatic dysfunction without chronic liver disease. Our study showed that all SALI in patients was caused by abdominal infection (intestinal fistula, abdominal trauma, and severe acute pancreatitis) without chronic liver disease. The blood and liver samples from SALI patients were obtained from the Department of Surgery in Shanghai Ninth People's Hospital.

Mice in this study

Male 6–8-week-old C57BL/6 mice (wildtype and Roquin-1$^{san/san}$) were supplied by the model animal research center at Nanjing University.

Cells and reagents

L929 cells were ordered from the ATCC (Manassas, USA). The Macrophage Isolation Kit and naïve T cell Isolation Kit was ordered from Miltenyi Biotec (Bergisch Gladbach, Germany). The plasmid and lentiviral were purchased from Hanheng Bio (Shanghai, China). Si-RNA was ordered from GenePharma (Shanghai, China). Lipofectamine 2000 reagent was purchased from Thermo Fisher (Haverhill, USA). The anti-mouse/human Roquin-1antibody was ordered from Invitrogen (California, USA). The primary mouse anti-mouse F4/80/CD11b/CX3CR1/Clec4F antibody and secondary antibody in immunofluorescence stains were purchased from Novus (Cambridge, USA). The antibodies in the flow cytometer were ordered from Biolegend (San Diego, USA). The antibodies and reagents in Western bolt analysis and immunoprecipitation were purchased from Abcam (Cambridge, USA). The primer and regents in qRT-PCR and Northern blot were ordered from Vazyme (Nanjing, China). ELISA kits were ordered from LiankeBio (Nanjing, China). The EVs and subcellular fraction isolation reagents were purchased from Beckman (Irvine, USA). The STAT3 inhibitor and AMPKα activator/inhibitor were ordered from MCE (Monmouth Junction, USA).

Chimeric mice

To construct the chimeric mice, we injected bone marrow-derived møs into mø-deficiency recipient mice by combinations of wild-type (C57BL/6NJ) and Roquin-1$^{san/san}$ mice in the recipient/donor combinations below: WT/WT, WT/San, San /WT, San/San. We performed the intraperitoneal injection of 200 μL liposome-encapsulated clodronate of 6-8 weeks wild-type and Roquin-1$^{san/san}$ mice before irradiation. Then, the mice were exposed to lethal 1000 cGy γ-ray for six hours before receiving 5 x 10^6 bone marrow-derived macrophages (BMDM) via tail vein injection.

Sepsis-induced liver failure model in mice

All the SALI patients in the study due to abdominal infection (intestinal fistula, trauma, and severe acute pancreatitis) and the result of the bacterial culture with peritoneal effusion included escherichia coli and klebsiella pneumonia. Thus, we used D-galactosamine (D-GalN) and lipopolysaccharide (LPS) to simulate the human condition to establish the SALI model in mice. 6-8 weeks, male mice were intraperitoneally injected with 0.8 mg/g D-GalN and 0.01 μg/ g LPS as previously described; meanwhile, the three control groups were separately administered the same doses of D-GalN, LPS or saline only. The mice were sacrificed for blood and liver tissue at different time points. Serum was used for biochemical analyses and ELISA before sacrifice. Liver tissue was collected for miRNA analysis, qRT-PCR, western blot and flow cytometry. The remaining tissues were used for histopathology and immunohistochemistry.

Macrophage isolation in mice liver

We used the MACS Macrophage Isolation Kit to isolate mø in mice. Specifically, we performed Percoll density gradient centrifugation to separate the mononuclear cell suspension. Then, FcR blocking solution was used to resuspend cells. Anti-Biotin Beads and Biotin-Antibody were added. After incubation, the magnetic bead sorting column was used for sorting.

Bone marrow-derived macrophage culture

The culture medium was rewarmed (the 929-cell culture supernatant was added) to 37°C. The mice were sacrificed and sprayed with 70% ethanol to separate the femur and tibia. A 20 ml sterile syringe was filled with prewarmed medium (929 cell culture supernatant) and used to flush bone marrow cells. The cell suspension was centrifuged and placed into a Petri dish. On the 4th day, we changed the culture medium. On the 7th day, the adherent cells were scraped off for further experiments.

Isolation of naïve T cells and induction of Tregs-differentiation

According to the instruction, we performed the negative selection of native T cells from the spleen in 6-8 week-old C57BL mice. Then, we stained cells with anti-CD4-FITC and used the FACS Canto II flow cytometer to analyze the purification.

The anti-CD3 antibody was used to precoat a 24-well cell culture plate overnight. Then, the cells were cultured with anti-CD28 (final concentration 2 μg/ml), TGF-β1 (final concentration 5 ng/ml) and IL-2 (final concentration 500 IU/ml) for 24 hours.

Primary hepatocyte sorting and culture in mice

The liver was harvested, milled, and filtered. The bottom layer cells were centrifuged at 50 g for two minutes, resuspended in 40% Percoll, and centrifuged at 200 g × 7 min. After centrifugation, the bottom layer of cells was washed and resuspended.

METHOD DETAILS

Macrophage-derived extracellular vesicles isolation

Briefly, cells were incubated in a serum-free medium for 48 hours. Then, we removed cells by spinning them at 50 g for 10 min. And cell debris was excluded by centrifuging at 2000 g for 25 minutes. Multivesicular bodies were isolated by centrifuging at 10,000 g for 30 minutes, and EVs were extracted at 100,000 g for 18 hours (or 2 hours). For density gradient purification, EVs were loaded on top of a 12 ml 5-40% discontinuous iodixanol density gradient and spun in an SW40 Ti rotary bucket rotor for 18 hours. Fractions were collected in a volume of 30 μl PBS.

For particle tracking analysis, each sample captured at least five 60-second videos. From these videos, calculate the average concentration and size of the particles and treat them as a physical copy. All duplicate settings and settings between different samples remain the same for normalization. The EVs concentration was calculated as particles/cells/hour of culture to obtain the EVs secretion rate.

For the concentration of small RNA in EVs, we extract the small RNA in EVs and detect the concentration of small RNA by NanoDrop. Meanwhile, we calculated the number of EVs. The small RNA volumes in EVs were calculated as small RNA volume(ng)/particle.

Coculture of møs/MDEVs and Tregs

At first, we coated the plate with anti-CD3 and anti-CD28 antibodies as previous protocol. TGF-β1 and IL-2 were added for Tregs differentiation. Meanwhile, we used 2×10^4 mφ or 2×10^6 MDEVs to stimulate T cells. After 24 hours, a FACS Canto flow cytometer was used to analyze the cells.

The absorption of MDEVs

We constructed the coculture of PKH67-labeled MDEVs and $CD4^+$ T cells for 24 hours. After 24 hours, we stained cells with PKH26. Then, we used Leica TCS SP8 confocal laser scanning microscope to analyze the samples.

Subcellular fractionation

The BMDM was starved for 18 hours and collected into a lysis buffer. To remove the nucleus in the lysate, we centrifugated the lysate at 10,000 xg for 30 minutes. The post-nuclear extract was loaded onto a continuous iodixanol density gradient and rotated in an SW40 Ti rotary bucket for five hours at 100,000 xg. To generate a 12 ml continuous iodixanol density gradient, 30%, 20%, 10%, 5%, and 2% iodixanol solutions were diluted in HB and covered from increasing to decreasing concentrations. The gradient was incubated overnight at 4°C to generate a continuous gradient, and the post-nuclear extract was loaded on top of the gradient. After centrifugation, fractions were collected and precipitated by StrataClean resin. The protein-bound StrataClean resin was pelleted by centrifugation and eluted by heating the beads in a loading buffer to 95°C for five minutes.

Plasmid construction

The vector sequence and primer synthesis were applied by Hanheng Biotechnology Co. The sequences in this study were listed in Table S3. We built A cDNA library to determine the target band. Then, we used a DNA recovery kit to collect the PCR product. Restriction endonucleases performed the digestion of the recovered PCR product and the plasmid.

Meanwhile, the target gene fragment and the vector fragment were produced. Then, the ligase reaction system was used to ligate the piece and the vector. Then, we transformed the ligation product into *E. coli* competent cells amplified the positive clones and extracted the plasmid for sequencing.

Point mutation plasmid construction

The point mutation plasmid was ordered from Hanheng Biotechnology Co., Ltd. The specific critical steps were listed in Table S4.

Lentiviral infection

We plated cells and grew them to 70% confluence. The virus solution was added to the cells and directly inoculated for four hours. Then, we changed the medium (without polybrene). After 72 hours, fluorescence microscopy was used to detect GFP.

Transfection of siRNA

The sequence of si-RNAs in our study is listed in Table S5. At first, the cells were plated in 24-well plates and grew to 70% confluence within 24 hours. Then, the diluted siRNA was incubated with the RNAi-Mate reagent for 20 minutes. Then, cells were incubated with siRNA/Lipofectamine complex for six hours. After six hours, we changed the medium. After 24 hours, further experiments were performed.

Suppressive activity of Tregs *in vitro*

At first, we stained the $CD3^{+}CD25$- T cells with CFSE dye. Co-culture was conducted according to proportions (Tregs: CD3+CD-25 T cells =1:4), and triplex pores were set for each condition. Four days later, the flow cytometer detected the T cells proliferation.

Immunoprecipitation

The lysate of cells was incubated with the antibody and protein A/G beads overnight. A magnetic stand was used to remove the supernatant. Then, we added the loading buffer and set samples in a 95°C-water for ten minutes.

Purified EVs resuspended in PBS were subjected to BCA analysis. Then 50 μg of EVs (200 μl volume) and 5 μg of mouse anti-CD63 antibody (IP: CD63) or 5 μg of normal mouse IgG (IP: IgG) for three hours. Then, the A/G magnetic beads were incubated with immunocaptured purified EVs. The supernatant was retained to analyze the pull-down efficiency. Magnetic beads were incubated with Laemmli sample buffer to elute protein. 10 μg of purified EVs were loaded as a 20% input compared with 20% of the supernatant on the blot.

The use of MDEVs, STAT3 and AMPKα activators/inhibitors

GW4869 is usually stored at -80°C as a 1.5 mM DMSO suspension. Control cells were treated with 5% MSA in DMSO, similar to the samples receiving the GW4869 solution. A certain amount of vesicle solution is added to equal the volume of GW4869 for 10 μM.

We dissolved Stattic (STAT3 inhibitor), Acadesine (AMPKα activator) and Compound C (AMPKα inhibitor) in DMSO at 10 mmol/L. For *in vitro* studies, Stattic, Acadesine and Compound C were dissolved to 10μM, 0.5mM and 2μM with medium, respectively.

Histology and immunofluorescence stains in tissue

For histology, the mouse tissue was fixed, embedded in paraffin and stained with hematoxylin+eosin. Then, microscopy and Suzuki's score were used to evaluate the tissue sections and analyze the injury size and morphology.

For immunofluorescence stain, anti-human/mouse RC3H1 mAb, anti-human CD11b mAb and anti-mouse F4/80/CX3CR1/Clec4F antibodies were used to detect the primary source of Roquin-1 in the liver. After incubation with a secondary antibody, DAPI was used to stain the cell nucleus. Then, we used Leica TCS SP8 Confocal Laser Microscope to analyze the samples.

Immunofluorescence stain in cells

We cultured cells on glass coverslips and used 100% methanol to fix the cells. Then, we incubate sections with the primary antibody at its optimal dilution for an hour. After washing with TBST, we counterstained twice for three minutes each with DAPI and used Confocal Laser Scanning Microscope to analyze the samples.

Transmission electron microscopy

The Formvar carbon film-coated grid was immersed in double-distilled water and 100% ethanol for washing. Then, we added the diluted sample to the grid and incubated it for one minute. Then, we stained the grid with phosphotungstic acid and air-dried it overnight. The grid was mounted on an FEI Tecnai T12 TEM (120kV LaB6 source), a Gatan cryogenic transfer stage, and a 2K x 2K CCD camera 2102 SC on the side of the AMT CR41-S and imaged.

RNA Binding Protein Immunoprecipitation (RIP)

We harvested BMDM, isolated nuclei and lysed nuclear pellets. Then, we immunoprecipitated Ago2 with the bound RNA and purified RNA bound to Ago2.

Flow cytometry

For analyzing the møs subset, we stained the cells with anti-F4/80-PE, anti-CD11b PE/Cy7, anti-CD11c-PerCP-Cy5.5 and anti-CD206-APC. Meanwhile, to measure the differentiation of Tregs, we labeled cells with anti-CD4-FITC, anti- CD25-APC, and anti- FoxP3-PE.

The stain was performed according to the protocol described by the manufacturer. Then, we used the FACS Canto II flow cytometer and Flow Jo v10.0.7 software to detect cells and analyze data.

Western blot analysis

We isolated protein with RIPA lysis buffer. The Bio-Rad protein assay quantified total protein levels. Then, proteins were loaded and separated by 10% or 8% SDS–PAGE and translated to the PVDF membrane. After incubation with primary antibodies, we incubated the membranes with HRP-conjugated secondary antibodies. Then, we used the chemiluminescence kit and Image Lab to detect and quantify the band.

MiRNA sequence assays

The sample was based on one ng to 2 μg of total RNA. We added 3 (Clontech mRNA-seq (for Illumina)) models at the 3′ end; samples were inverted by the addition of oligo(dT) primer, and a specific sequence was added at the 3′ end of the 1st cDNA by TSO primer (Clontech mRNA-seq (for Illumina)). Library enrichment and addition of Illumina sequencing sequence (PCR 7-17 cycles) (Clontech mRNA-seq (for Illumina)) were performed. Library purification was performed. TBS380 (Picogreen) quantitative analysis was performed and mixed based on the data. Bridge PCR amplification on cBot was performed to generate clusters. The HiSeq2500 sequencing platform was used for 50 bp sequencing. The data was uploaded to the databank (GSE169215). Then, to identify differentially expressed genes, we employed a count-based negative binomial model implemented in the software package Dseq2.[66] Considered differentially expressed were genes with an adjusted (Benjamini and Hochberg method) p value 0.05 indicating altered expression. Meanwhile, ggseqlogo[67] package was used to investigated the sequence logos.

Qualitative RT-PCR analysis

We extracted total RNA from organs and cells according to the manufacturer's protocol. HiScript Q RT SuperMix kit was used for reverse transcription (Table S6). Then, for Real-time quantitative PCR analysis (RT-qPCR), we used the SYBR RT-PCR kit and Light-Cycler 480II Real-Time PCR system.

ELISA

With the product instruction, ELISA kits were used to examine the serum ALT/AST and the inflammatory profile (IL-6, IL-10, TNF-α, and TGF-β) in serum and supernatant.

miRNA pulldown

BMDM were scraped and treated in hypotonic lysis (HL) buffer, 5% glycerol, 0.5% NP-40, and protease inhibitor 25 L avidin beads per sample were washed twice in HL buffer and conjugated with 22nt-polyA. To accomplish this, they were treated with 5 nmol 22nt-polyA, 1 mg/mL yeast tRNA, 5 mg/mL ultrapure BSA, and 1 L/mL RNasin ribonuclease inhibitor in hypotonic lysis buffer for 2 hours and thirty minutes. The polyA-conjugated avidin beads were incubated with cell lysates for 6 hours at 4°C with constant rotation before being centrifuged twice at 1,500 g to remove the beads. Lysates were incubated overnight at 4 degrees Celsius with avidin beads conjugated to one of the miRNAs, and 22-nt-polyA in the presence of 1 L/mL RNasin ribonuclease inhibitor. All constructs, including 22nt-polyA and scramble miRNA, contained a 5′-biotin group immediately followed by a Spacer9 sequence. 25 avidin beads/sample were incubated with 5 nmol of one of each of the aforementioned constructs, 1 mg/mL yeast tRNA (Sigma), 5 mg/mL ultrapure BSA, and RNasin ribonuclease inhibitor in hypotonic lysis buffer for 6h at 4°C, followed by two washes in HL buffer.

After overnight incubation, beads were recovered by centrifugation at 1,500 g and successively washed in HL buffer, HL buffer containing 100 mM KCl, HL buffer containing 200 mM KCl, and PBS. In all phases, an RNasin inhibitor was added to the buffers. The beads were treated with a 5 mM biotin solution in continuous rotation for 45 min to elute proteins attached to miRNA-conjugated beads. The supernatants were collected and precipitated with trichloroacetic acid.

Luciferase assay

BMDM and $CD4^+$ T cells were cultured in 24-well plates for 24 h. TSC22D2 reporter luciferase plasmid (100 ng), pGL3-TSC22D2-3′UTR (wt/mut), control luciferase plasmid, and 5 ng pRL-TK Renilla plasmid were transfected into the cells using Lipofectamine 2000. After 48 h, the Dual-Luciferase Reporter Assay Kit (Promega) was used to analyze Luciferase and Renilla signals.

Study approval

The Office approved the protocol for this study of Research and Ethics at Shanghai Jiaotong University Affiliated 9th Hospital (SH9H-2019-TK199-1). Informed consent was obtained from the patients. Human samples were used by the NIH and institutional guidelines for human subject research. The Animal Care and Use Committee in Shanghai Jiaotong University Affiliated 9th Hospital approved the experiment protocol in mice.

Statistical analysis

Data are expressed as the mean ± standard deviation (S.D.). The Mann–Whitney U test, Student's t-test, and one-way ANOVA were performed to compare treatment groups. Correlation between Roquin-1 and pro/anti-inflammatory profile analyzed by non-parametric Spearman's method. Statistical analysis was performed using SPSS 22.0 and GraphPad Prism 8. A p-value <0.05 was considered statistically significant. p<0.01*, p<0.01 **, p<0.001 ***, p<0.0001 ****.

QUANTIFICATION AND STATISTICAL ANALYSIS

Data are described as the mean ± standard deviation (S.D.). The Student's t-test and one-way ANOVA were performed to compare the difference between groups. The correlation between Roquin-1 and the pro/anti-inflammatory profile was analyzed by non-parametric Spearman's method. Statistical analysis was performed by SPSS 22.0 and GraphPad Prism 8. A *p*-value <0.05 was considered statistically significant. *p*<0.01*, *p*<0.01 **, *p*<0.001 ***, *p*<0.0001 ****.